A QPSK 110-Gb/s Polarization-Diversity MIMO Wireless Link With a 220–255 GHz Tunable LO in a SiGe HBT Technology

Pedro Rodríguez-Vázquez, Janusz Grzyb, Bernd Heinemann, and Ullrich R. Pfeiffer, *Fellow, IEEE*

***Abstract*— In this article, a polarization-diversity technique multiple-input multiple-output (MIMO) is demonstrated to double the spectral efficiency of a line-of-sight quadrature phase-shift keying (QPSK) wireless link at 220–255 GHz with a pair of highly integrated single-chip transmitter (TX) and receiver (RX) front-end modules in 0.13-μm SiGe HBT technology (f_T/f_{max} = 350/550 GHz) exploiting only a low-cost wire-bonded chip-on-board packaging solution for high-speed baseband (BB) signals. Both TX and RX chips accommodate two independent fundamentally operated direct-conversion in-phase and quadrature (IQ) paths with separately tunable on-chip multiplier-based (×16) local oscillator (LO) generation paths driven from a single external highly stable 13.75–16-GHz frequency synthesizer. On the RX side, a mixer-first architecture is implemented to improve the symmetry between upper and lower sidebands (USB and LSB) at the cost of an increased noise figure (NF), whereas, on the TX chip, each upconversion mixer is followed by a gain–bandwidth (BW)-limited four-stage power amplifier (PA) to support the link budget at a meter distance. Next, two independent IQ data streams from the upconversion/downconversion paths on each chip are directed to a common lens-coupled broadband on-chip slot antenna system. This way, two orthogonal circular polarizations [left-handed circular polarization (LHCP) and right-handed circular polarization (RHCP)] can be transmitted with sufficient isolation for link operation without the need for a high-speed depolarizer in the BB for any relative orientation between TX and RX modules. The antenna combined with a 9-mm diameter Si-lens provides a directivity of 23.5–27 dBi at 210–270 GHz for each of the modules. This, along with a peak radiated power of 7.5 dBm/ch from the TX module, and the cascaded conversion gain (CG)/single sideband (SSB) NF of 18/18 dB/ch for the RX module followed by a broadband amplifier (PSPL5882) from Tektronix allowed successful transmission of two independent QPSK data streams with an aggregate speed of 110 and 80 Gb/s over 1 and 2 m, respectively, at 230 GHz with a board-level limited channel BB bandwidth (BW) of 13.5 GHz.**

Manuscript received November 19, 2019; revised February 5, 2020; accepted March 14, 2020. Date of publication June 5, 2020; date of current version September 2, 2020. This work was supported in part by the Deutsche Forschungsgemeinschaft (DFG) Schwerpunktprogramme (SPP) 1655 Real100G.RF2 and in part by the EU 316755 DOTSEVEN Project. *(Corresponding author: Pedro Rodríguez-Vázquez.)*

Pedro Rodríguez-Vázquez, Janusz Grzyb, and Ullrich R. Pfeiffer are with the University of Wuppertal, 42119 Wuppertal, Germany (e-mail: rodriguezvazque@uni-wuppertal.de; grzyb@uni-wuppertal.de; ullrich.pfeiffer@uni-wuppertal.de).

Bernd Heinemann is with IHP-Leibniz-Institut für innovative Mikroelektronik, 15236 Frankfurt, Germany (e-mail: heinemann@ihp-microelectronics.com).

Color versions of one or more of the figures in this article are available online at http://ieeexplore.ieee.org.

Digital Object Identifier 10.1109/TMTT.2020.2986196

***Index Terms*— Circular polarization, high-speed terahertz communication, multiple-inputs multiple-outputs (MIMO) communication, polarization-diversity antenna, quadrature phase-shift keying (QPSK), SiGe HBT.**

I. Introduction

In RECENT years, the demand for high data-rate wireless links has grown exponentially. At lower carrier frequencies with congested bandwidth (BW), high-complexity high-order modulation is pushed to the limits to improve the speed of current communication systems. Driven by the demands of the future networks, the need for larger communication BW in both indoor short-distance and outdoor large-distance point-to-point wireless links becomes evident, thus motivating a gradual shift of carrier frequencies toward higher mmWave band. Carriers in the near-terahertz transmission window beyond 220 GHz with still vast available spectrum are anticipated by the new IEEE 802.15.3d-2017 [1] standards as promising for the realization of future 100+ Gb/s data rates [2]–[4]. The future 6G networks are envisioned to operate in this frequency range with expected data rates approaching 1 Tb/s [5]. However, a straightforward increase of absolute BW with the carrier upscaling becomes unrealistic because multiple limitations of current semiconductor, packaging technologies are reached, and further speed improvements become very challenging.

The majority of the currently available radio frequency (RF) front-end solutions for near-terahertz fully electronic wireless communication relies on III–V semiconductors with impressive peak f_{max} exceeding 1 THz [6]–[8] but featuring a low level of integration in expensive split-block waveguide packaging with external aperture antennas [9]–[14]. Here, both short-distance and external optics-supported long-distance links with modulation speeds of up to 96 and 100 Gb/s have been demonstrated for 8-PSK (phase shift keying) and 16-QAM (quadrature amplitude modulation) modulation formats, respectively [9], [10].

Contrary to III–V solutions, silicon technologies promise high integration levels, including future digitally assisted baseband (BB) processors. Still, the circuit performance deteriorates at an accelerated speed while operating above 200 GHz due to a limited device gain–BW product and an increased noise figure (NF) in close proximity of f_t/f_{max}. This leads to

not only poor power efficiency and tight link budget but also results in a very limited scaling of the BW with the carrier frequency increase and a considerable asymmetry between lower and upper sidebands (LSB and USB) [15], [16]. Such deficiencies become particularly pronounced for CMOS technologies [17], [18], where fundamentally operated architectures are not readily available, and massive power combining needs to be applied for any reasonable transmitted power levels [19]–[24]. Although SiGe HBT devices potentially promise a relaxed link budget [25]–[27] for transceiver operation near 200 GHz and above, the so far reported SiGe-based wireless experiments have been predominantly performed in a low cm-range distance and/or under wafer-probing conditions without packaging [19]–[24], [28]–[31]. Here, on-chip integration of antenna elements, although challenging for silicon technologies, shows an underestimated benefit in terms of considerably reduced packaging costs for terahertz-signal escape [15], [24], [28], [30], [32]–[35]. In this article, a low-cost wire-bond chip-on-board (COB) packaging in combination with a silicon lens-integrated on-chip antenna was applied to demonstrate a 1-m distance wireless transmission at 220–260 GHz for two independent direct-conversion quadrature transceivers in 0.13-μm SiGe HBT with the highest modulation format of 64 QAM [36]–[39] and the peak data rate of 100 Gb/s for 16 QAM [15], [40].

Independently of the semiconductor technology in use, speeds of 100 Gb/s and above can be approached by increasing either the modulation order or the modulation BW. With an increase of the modulation format, the requested modulation BW is lower, but the tolerable aggregate level of static and BW-related impairments also shrinks very quickly, becoming unrealistic at near-terahertz frequencies considering the feasible link budget constraints. In particular, a realistic phase error in the local oscillator (LO) generation path, scaling not only with carrier frequency but also with modulation BW [39], [41], [42], may prevent any higher modulation format for a fully electronic transceiver. Furthermore, for effective implementation of higher order modulation, a sufficient digital-to-analog and analog-to-digital converter (DAC/ADC) resolution needs to be provided at the sampling speed as high as twice the baud rate. A 6-bit effective resolution is typically needed for pulsed-amplitude modulation (PAM4), which becomes extremely challenging to achieve with 10+ GHz BW due to the limited dynamic accuracy and challenging sub-ps timing control [43].

Contrary to that, a high-speed quadrature phase-shift keying (QPSK) requires only a 1-bit digital-to-analog (D/A) interface and can potentially be operated up to the baud rate [43], therefore considerably relaxing the speed and linearity requirements of D/A interface. The penalty to pay for that is an increase of effective channel BW, which may be equally limited by bandpass response of RF blocks as well as low-pass (LP) characteristics of high-speed packages in the BB path. Despite the larger requested BW, a high data-rate operation may be easier to achieve due to the relaxed linearity and phase error tolerance.

Considering that both methods of approaching the targeted 100+ Gb/s speed by increasing either modulation order or modulation BW at near-terahertz carrier frequencies face multiple challenges related to practical hardware limitations, two additional techniques can be further investigated to increase a total aggregate modulation speed. These are spatial/polarization orthogonality and channel bonding; both, although commonly applied at lower operation frequencies [44]–[48], have not been extensively exploited in prior work on broadband communication at near-terahertz carrier frequencies. Polarization diversity with two linearly polarized on-chip antennas was demonstrated for a 220-GHz amplitude shift keying (ASK) transmitter (TX) to increase a total data rate to 24.4 Gb/s over a 10-cm distance [28]. The use of linear polarization, however, requires accurate relative polarization alignment between TX and receiver (RX) for sufficient leakage suppression between two transmission paths. Such a setup becomes impractical in real application scenarios and requires the use of a depolarizer circuit in the BB [47], the implementation of which at 100+ Gb/s speeds may become challenging if not impossible. Contrary to that, simultaneous transmission of two circularly polarized orthogonal waves can potentially be applied to increase the link spectral efficiency for any relative orientation between TX and RX and without the use of a high-speed BB depolarizer under the provision that sufficient isolation between two adjacent transmission paths in the entire modulation BW can be achieved.

This article demonstrates the feasibility of doubling the spectral efficiency of a line-of-sight QPSK wireless link by applying polarization orthogonality to a pair of highly integrated fundamentally operated direct-conversion in-phase and quadrature (IQ) modules with a tunable carrier of 220–255 GHz. Both TX and RX modules are implemented as single-chip solutions in 0.13-μm SiGe HBT technology in combination with a wire-bonded COB packaging for high-speed BB signaling and an on-chip radiator interface to free space. Each of the TX and RX chips accommodates two independent upconversion/downconversion channels connected to a single silicon lens-coupled on-chip antenna supporting two orthogonal circular polarizations—right-handed circular polarization (RHCP) and left-handed circular polarizations (LHCP)—with sufficient isolation to implement a polarization-diversity multiple-input multiple-output (MIMO) over large modulation BW. The chipset in combination with a 9-mm diameter hyperhemispherical Si-lens, providing a directivity of 23.5–27 dBi at 210–270 GHz for each of the modules, successfully demonstrates a simultaneous transmission of two independent QPSK data streams, 55 Gb/s each, over a 1-m line-of-sight distance with an error vector magnitude (EVM) of 31.9% under a board-level limited channel BB BW of 13.5 GHz.

This article is organized as follows. Section II presents a top-level system description and an analysis of the influence of the polarization leakage on the link quality, measured as bit error rate (BER)/EVM. Section III describes the implementation details for all relevant functional blocks in the transmit and receive paths. In Section IV, relevant RF measurements for the dual-polarization (DP) TX and RX front-end modules operating individually and in a back-to-back configuration are

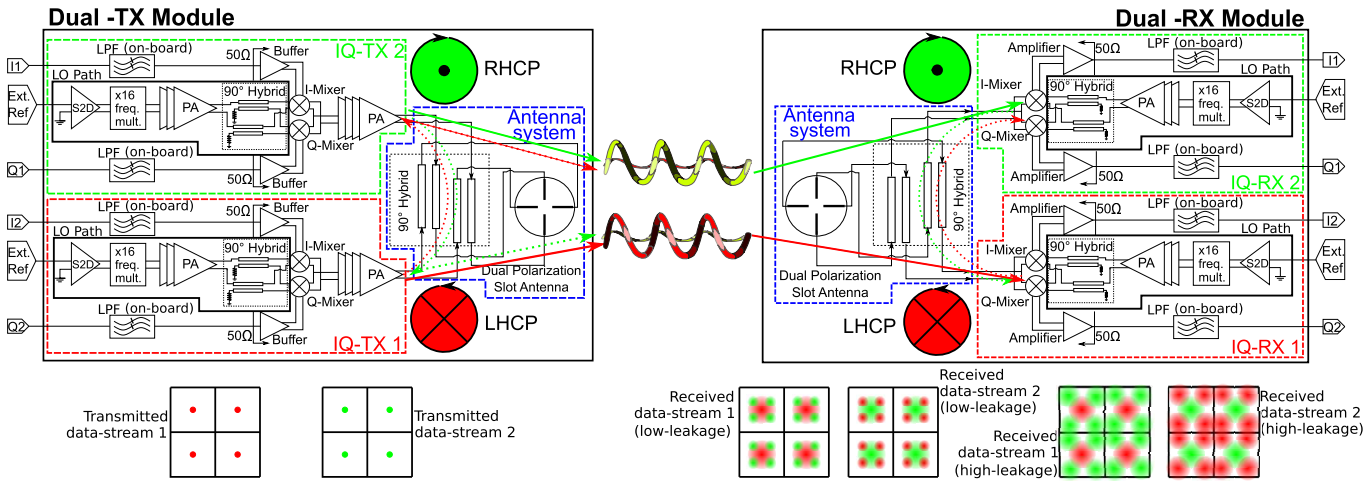

Fig. 1. Top-level architecture of the DP TX and RX modules in a back-to-back wireless configuration with the indicated two orthogonal transmission paths (RHCP and LHCP). Two major sources of finite isolation between both paths are also sketched. These are the antenna XPD and a direct leakage between the antenna RHCP and LHCP driving ports on each of the TX and RX modules.

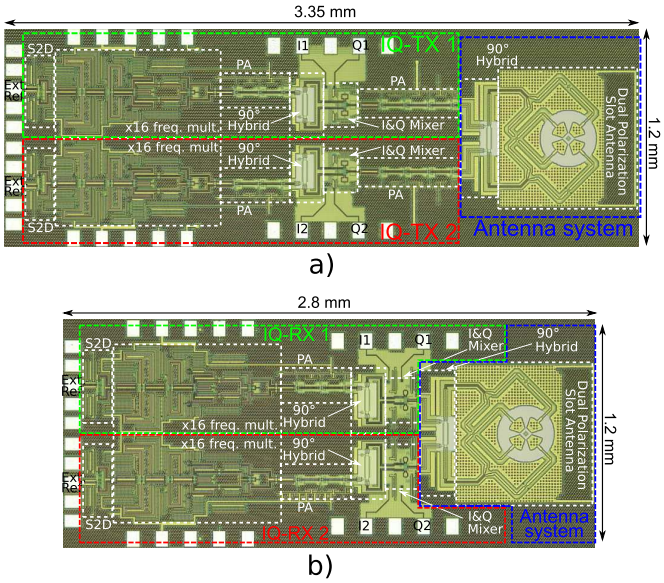

Fig. 2. Chip micrographs of (a) TX and (b) RX.

presented. Section V demonstrates the MIMO operation of the wireless link. Finally, conclusions are drawn in Section VI.

II. Top-Level Architecture of TX and RX

A top-level block diagram of the DP TX and RX modules in a back-to-back link configuration is shown in Fig. 1. Both TX and RX chips consist of two independent transmit/receive paths, respectively, placed side-by-side, as shown in Fig. 2. A circularly polarized on-chip antenna system combines the modulated data from both paths on each chip with two input ports supporting orthogonal, RHCP and LHCP, polarizations. Each of the TX/RX channels represents a circuit architecture topologically similar to our previous work [15], [40] featuring an externally driven $\times 16$ multiplier chain in the LO generation path and a mixer-first arrangement on the RX side for improved symmetry between USB and LSB. In the current chip implementation, both channels possess separate LO paths, which allows the investigation of the on-chip leakage mechanisms between them, as will be explained in Section III. The antenna is an extension of our previous implementation in the 240-GHz frequency-modulated continuous-wave (FMCW) radar [32], [33], [49], [50], wherein a large instantaneous fractional BW was not required. The primary radiator is an annular slot with two pairs of orthogonal feeds providing polarization diversity, which, in combination with a quadrature hybrid driving those feeds, supports two orthogonal circularly polarized waves (see Figs. 1 and 2). The antenna is coupled to a silicon hyperhemispherical lens to minimize the influence of substrate modes in a silicon chip and to increase the antenna directivity.

For the maximum data rate in the overall polarization-diversity MIMO system, the hardware impairments inherent to each of two transmission channels as well as isolation between them need to be carefully considered. The coupling between two orthogonal data streams takes place predominantly on the antenna level. Here, the aggregate isolation is determined by two main factors on each side of the link: 1) direct leakage between two antenna driving ports and 2) antenna cross-polarization level (XPD), as indicated with dotted lines in Fig. 1. For the circularly polarized waves, the XPD in dB can be expressed in terms of axial ratio (AR) [51], [52] as

$$\text{XPD (dB)} = 20\log_{10}\left(\frac{\text{AR}+1}{\text{AR}-1}\right). \tag{1}$$

In a back-to-back wireless link, the cross-polarization-incurred isolation is a function of the RF frequency and the relative alignment between the major and the minor polarization axis on both sides. In the worst case scenario, it is a twofold value of XPD under the assumption of equal polarization purity for both RHCP and LHCP on both ends of the link. A direct leakage between the RHCP and LHCP driving ports of the antenna system, in particular, in the presence of substantial impedance mismatch between the antenna and the circuit

blocks, may further lead to parasitic transmission/reception at the complementary polarization. The overall isolation is the primary design requirement and needs to be provided over the entire RF BW and for any relative orientation between TX and RX modules.

On top of the regularly considered figures of merit, such as output power, NF, or IQ imbalance, the major performance-limiting imperfections of each single-polarization channel, separately, further include: 1) nonidealities in the LO generation path such as near-carrier and far-out phase noise with implementation-specific harmonic spurs and 2) BW-limited LP BB and bandpass RF response limitations with frequency-dependent amplitude and group delay distortions.

The EVM will be used as a standard and a modulation format-independent metric of the link quality [53], [54]. The contribution of the above-listed system-level impairments will be added in an aggregate EVM [55], assuming that they are statistically independent. Under the assumption of the XPD with a white frequency distribution in the operation BW [56], the cross-polarization-incurred isolation will set the minimum EVM in the absence of other link impairments, limiting the maximum modulation order of the system.

III. Block-Level Description of DP TX and RX Modules

In this section, the implementation details for all relevant functional blocks in the transmit and receive paths are presented, particularly addressing design aspects that stay in direct relation to the top-level link imperfections described in Section II. As the primary topic of this article is on the MIMO operation, the design details related to each separate transmission path with its inherent impairments will be treated briefly and with the main focus on the characterization results.

A. Circuit-Level Description of the Single-Polarization Path

Due to the large instantaneous BW required for 100+ Gb/s data rates, the influence of both the RF bandpass response and the LP characteristics of high-speed BB interface for both transmit and receive paths needs to be traded against each other resulting in some specific choice of transceiver architecture. Both of them set the effective BW of a complete link in a back-to-back configuration (TX_{BB}-to-RX_{BB}) and, in combination with a suitable packaging solution, need to provide both the minimum frequency-dispersion (amplitude and group delay) high-speed BB signaling and the high-fidelity, low-loss interface to free space at a near-terahertz carrier frequency. Considering the practical package-level BW limitations, as discussed in Section III-B, a direct-conversion IQ transceiver architecture is beneficial compared with a heterodyne intermediate frequency (IF) topology, wherein a large modulation BW needs to be accommodated on top of an IF frequency, not only for the analog part but also for the ADC/DAC and digital signal processing (DSP) blocks that, additionally, should preserve the phase information of bandpass-modulated signals. This benefit, however, comes at the cost of some other challenges, which may considerably influence the performance of a single transmission channel.

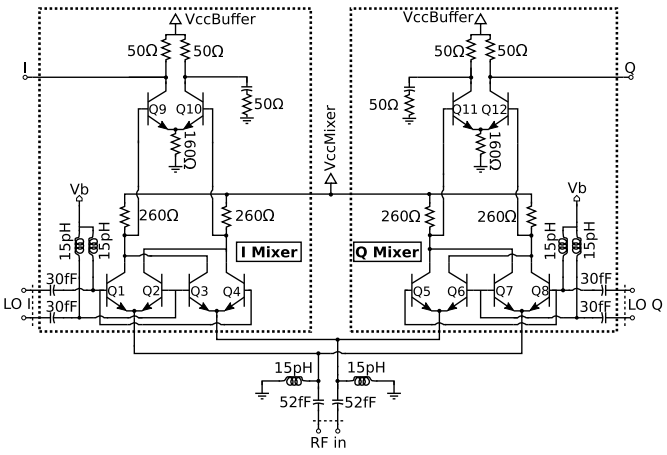

Fig. 3. Circuit-level schematic of the double-balanced IQ switching-quad downconversion mixer, including the BB amplifier. The emitter area for each of Q1–Q12 is $2 \times (1 \times 0.1)$ μm^2. One side of the differential outputs is terminated to facilitate a single-ended operation with the limited measurement equipment.

One of the most, if not the most, important is the necessity of IQ operation at RF frequency [15], [16], which is removed with an IF architecture. It leads to potentially substantial leakage between I and Q channels that may dominate other impairments and limit the achievable data rates despite a sufficient arbitrary white Gaussian noise-defined (AWGN) signal-to-noise ratio (SNR). This issue is related to a double-sideband quadrature upconversion/downconversion in the RF path and is a direct consequence of insufficient symmetry between USB and LSB (amplitude and phase) in both TX and RX blocks over large instantaneous modulation BW [15].

1) Downconversion and Upconversion Paths: On the RX side, a mixer-first architecture [15], [40] is implemented to improve the symmetry between USB and LSB, which was found insufficient in our previous amplifier-first RX [36]–[39] due to the limited device gain–BW product in the amplification stages [15], [40], [57]. This comes at the 2-dB noise degradation. A double-balanced fundamentally operated IQ switching quad topology (Q1–Q8) followed by a differential amplification stage (Q9–Q12) in the BB path matched to $2 \times 50\ \Omega$ is implemented for broadband operation in the entire LO range of 220–260 GHz, as shown in Fig. 3. For simultaneous optimization of conversion gain (CG) and NF, the mixer is biased at low current and driven with 4–5-dBm LO power through a broadband quadrature coupler, i.e., the same one used in the antenna system (see Section III-C). The internal nodes shared by the mixer and the amplifier stage set a compromise between CG, NF, and BB BW while neglecting package-related BW constraints. For further details on the mixer design, please refer to [40]. The simulated RF/LO 3-dB BW is 47 GHz. Due to BW limitations of the wire-bond COB packaging solution, the RX 3-dB BB BW is limited to around 14 GHz (see Sections III-B and IV-B) with a simulated in-band group delay variation of ± 10 ps, dominated by the compensating onboard filter at the BB pads [40]. The downconversion stage dissipates 70 mW.

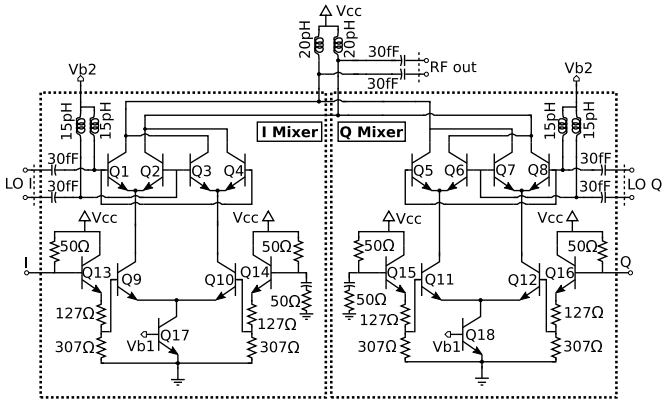

Fig. 4. Circuit-level schematic of the double-balanced IQ Gilbert-cell upconversion mixer. The emitter areas for Q1–Q8, Q9–Q12, and Q13–Q18 are $1 \times (1 \times 0.1)\ \mu\text{m}^2$, $2 \times (1 \times 0.1)\ \mu\text{m}^2$, and $4 \times (1 \times 0.1)\ \mu\text{m}^2$, respectively. One side of the differential BB inputs is terminated to facilitate a single-ended operation with the limited measurement equipment.

Opposed to the RX chip, each upconversion mixer is followed by a gain–BW-limited differential four-stage cascode power amplifier (PA). This topology is similar to [58] and supports a link budget for a meter distance. However, this PA generates LSB/USB asymmetry. As the PA block is not tunable, the asymmetry shows an LO frequency dependence. Here, a classical double-balanced fundamentally operated IQ Gilbert-cell mixer (see Fig. 4) is implemented. Similar to the RX, it is switched with 4–5-dBm LO power through a quadrature coupler. The high-speed IQ BB signals are provided to the mixing core (Q1–Q8) from the board level through the buffered ($2 \times 50\ \Omega$) differential transconductance stages (Q9–Q10 and Q11–12) and are subject to the same package-level BW limitations as the RX block, with a simulated 3-dB RF/LO BW of 35 GHz centered at 235 GHz. A group delay variation in the TX RF path is dominated by the PA and was simulated to be 75 ps with a variation of ± 7 ps in the operating BW. This PA presents a simulated small-signal gain of 12.5 dB, a BW of 30 GHz centered at 240 GHz, and a saturated output power of 9.5 dBm. The upconversion stage and the PA dissipate 140 and 450 mW, respectively.

Due to the limitations in the number of available lab equipment quantity to simultaneously drive four high-speed differential BB signals on each link side, the RX BB outputs (Q9–Q12) and TX inputs (Q13–Q16) needed to be operated as single-ended (terminated Q10–Q11 and Q14–Q15 on RX and TX sides, respectively) with a degraded balance in the output/input amplification stage resulting in a deteriorated SNR as well as an increased frequency dispersion in the operation BW.

2) LO Generation Path: Besides the abovementioned frequency-dependent distortions of the effective channel BW, the LO generation path is also prone to multiple limitations with a direct influence on the wireless transmission although ideal LO signal is considered a single tone and, thus, not influenced by the BW-related distortions. As opposed to narrowband channels at low frequencies with low near-carrier phase noise available, the LO phase error deteriorates quickly not only by carrier frequency upscaling to the near-terahertz band but also due to the influence of a broadband LO noise floor in the LO generation path scaling nearly linear with the modulation BW [41], [42]. To minimize this phase error and to provide wideband LO tunability for investigation of the frequency-dependent channel distortions, the on-chip LO path is implemented by a tunable $\times 16$ frequency multiplication of a high-stability external Keysight E8257D synthesizer with an excellent single-sideband broadband noise floor of -150 dBc/Hz at 15 GHz. The multiplication factor was chosen as a compromise between the limited RF performance of the wire-bond interconnection and the circuit implementation complexity. Assuming ideal noise scaling of $20\ \log_{10}(16) = 24.1$ dB by upconversion to 240 GHz, an rms phase error of around 5° is already anticipated for a 15-GHz range BB BW [16], [39], which sets a practical upper boundary on the modulation format around 64-QAM.

An inherent drawback of the chosen LO generation method with a high multiplication factor is the potential presence of false BB replicas in a spectral distance equal to integer multiples of an external LO drive frequency, which is 13.75–16.25 GHz in the current implementation. For sufficiently high data rates, these replicas alias with the main modulation spectrum with no space for filtering at the RX output and, therefore, should be sufficiently suppressed for successful demodulation. The LO path, topologically similar to that from [58], consists of an active input balun with four cascaded double-balanced Gilbert-cell doublers followed by a three-stage cascode PA providing around 4–5-dBm power within 220–260 GHz to each of the IQ mixers. Despite a double-balanced operation of the $\times 16$ chain, some parasitic spurious phenomena were identified, which are related to unsatisfactory attenuation of the externally supplied 13.75–16.25-GHz LO driving signal and its harmonics traveling across the chip ground plane. The first is its insufficient isolation directly at the RX BB ports, which was measured at a -50 to -55 dBc level and already found to influence the quality of a 1-m distance link (80-dB path loss at 240 GHz) for modulation BW reaching the external LO tone [15]. The other is the presence of both odd $\times 15$ and $\times 17$ and even $\times 14$ and $\times 18$ harmonics around the desired $\times 16$ spectral line. The odd harmonic spurs are particularly harmful to the link performance at higher modulation speed due to the lowest spectral distance to the desired $\times 16$ LO carrier.

In the current implementation, each chip features two independent LO paths, driving two separate transmission channels (see Fig. 1), which is explained in the following sections (see Section III), and can be used to characterize the direct on-chip leakage between two driving ports of the antenna system. In the wireless link experiment, both LO paths are operated at the same frequency. Each LO generation path dissipates 370 mW, and in a future redesign, they may be replaced by a single one to reduce the power consumption.

B. Packaging

A low-cost COB packaging solution is used to provide all dc, LO driving tone, and high-speed-modulated BB signals

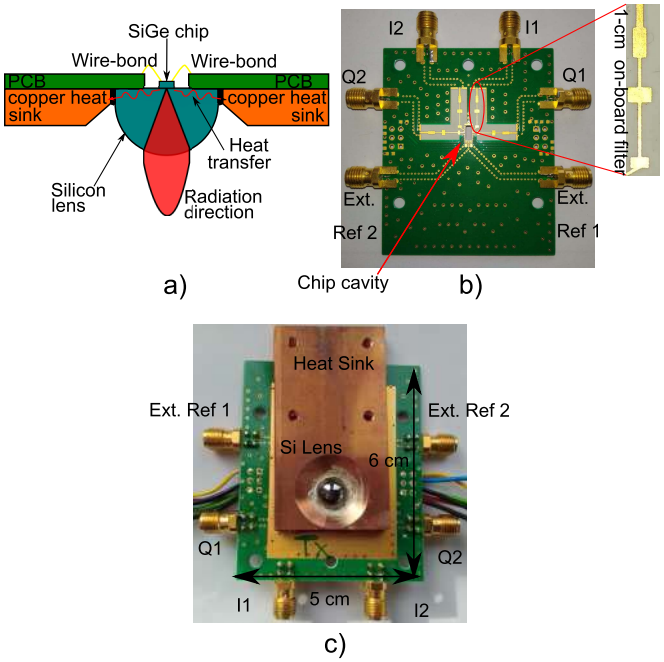

Fig. 5. (a) Cross-sectional view of the chip-on-lens assembly in the PCB recess. (b) Photograp of the PCB with the LO and BB signal distribution, including the LP filter for wire-bond compensation. (c) Photograph of the completely assembled TX front-end module.

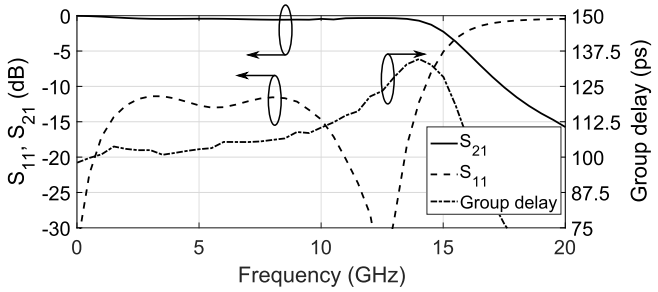

Fig. 6. Simulation results of a single interconnection path between the board connector and the on-chip BB input/output pad, including the ON-board LP filter [40].

on the board level. Here, each of the TX and RX chips is mounted on the backside of a 9-mm-diameter hyperhemispherical lens made of high-resistivity silicon with the primary on-chip radiator aligned with the lens center. The volume of a 9-mm lens provides sufficient thermal control for the chips dissipating between 0.9 and 1.95 W. The on-chip heat is further transported through the lens to a heat-sink attached to the printed circuit board (PCB) bottom side. The overall chip-on-lens assembly is placed in a recess of a regular two-layer 0.5-mm-thick Rogers 4350 B board surrounded by a metal plane, as shown in Fig. 5. No antireflection coating on the lens aperture is currently provided, which has an influence on the operation of both TX and RX modules and is discussed in more detail in Section III-C. If desired, the overall antenna directivity can be adjusted with no need for any on-chip redesign, simply by changing the lens dimensions to accommodate different link budget constraints.

Only a manual mm-length wire-bonding process was applied to all on-chip connections. With the limited dimensional control of the wire, the bonding process, altogether with the RF connector assembly tolerance, is not only a nonnegligible source of mismatch between all 4 I and Q BB paths but also leads to asymmetry in each of the differentially driven BB input/output signals. To minimize the influence of mm-long wire bonds on the package-level BW, an eight-section step-impedance microstrip-line LP filter, similar to that from [40], is implemented onboard for each of the high-speed BB signals, as indicated in Fig. 5. The filter embeds the wire bond inductance as one of its eight constitutive elements, reducing the influence of the asymmetry of the assembly process in the resulting BW. A Butterworth topology was chosen as a compromise between the 3-dB BW, group delay flatness, and the PCB size [59]. The simulation results of a single interconnection path between the board connector and the on-chip BB input/output pad are shown in Fig. 6. A 14-GHz BW with a group delay in-band variation lower than 37.5 ps is simulated. Due to the large electrical size of the compensated BB interconnection, the package-level incurred group delay variation was found to dominate a global group delay distortion of the entire back-to-back link (TX_{BB}-to-RX_{BB}).

C. Antenna System

The antenna system needs to provide both low-frequency dispersion of the digitally modulated high-speed signals as well as sufficient isolation between both transmitted data streams over large RF operation BW. The group delay between the antenna driving ports and free space needs to be preserved to minimize the frequency dispersion, and a combined directivity of the lens-coupled TX and RX antennas should compensate for the frequency-increasing free-space path loss, according to the well-known Friis transmission equation. The isolation, as previously mentioned in Section II, is defined mainly by the antenna axial ratio and direct leakage between the antenna driving ports.

The complete antenna system, as shown in Figs. 7 and 8, comprises a cascaded connection of the wideband differential 100-Ω quadrature coupler and the main radiating annular slot illuminating a hyperhemispherical silicon lens through the backside of a 150-μm-thick silicon die with a bulk resistivity of 50 $\Omega \cdot$ cm [49], [50]. The main radiator supports two orthogonal linear polarizations excited by two pairs of patch probes, P1–P2 and P3–P4, located 90° apart along the slot circumference [32], [33] driven in quadrature from two input ports—LHCP and RHCP—of the coupler. The antenna is embedded in a seven-layer 12-μm-thick back-end-of-line (BEOL) stack of a silicon chip. In the following, the most relevant implementation details for each of all constitutive components of the antenna system will be briefly presented in view of the abovementioned key requirements.

1) 3-dB Differential Quadrature Coupler: The coupler directly interfaces the IQ TX/RX circuitry (IQ1 and IQ2 in Fig. 1) with the main radiator, and therefore, its inherent isolation between input ports (LHCP and RHCP), phase

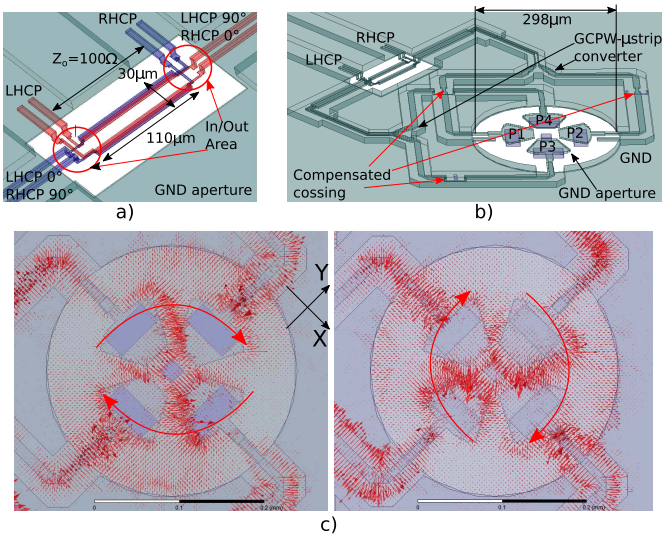

Fig. 7. 3-D simulation models of (a) quadrature coupler with the RHCP and LHCP driving ports, (b) complete antenna system, and (c) E-field distribution in the BEOL stack around the slot radiator at 240 GHz for two chosen excitation phases of the RHCP polarization advancing each other by 90°.

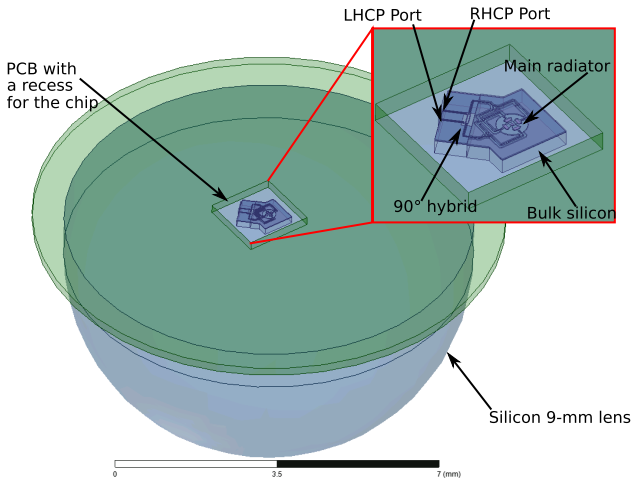

Fig. 8. 3-D simulation model of the packaged RF module with a silicon chip on the backside of a 9-mm silicon lens. The lens is attached to the metalized PCB, whereas the front-end hip sits inside a rectangular recess. A magnified view of the on-chip antenna system is shown in the inset.

and amplitude imbalance between two output ports (LHCP 0°/RHCP 90° and LHCP 90°/RHCP 0°), and matching at all four ports across the entire RF BW are essential for the leakage between both communication channels. The coupler exploits both broadside and edge coupling between four buried 110-μm long strip conductors with the ground plane underneath locally removed for appropriate control of the even/odd mode impedances to ensure maximum operation, whereas the feed lines are implemented as 100-Ω grounded coplanar striplines (GCPS) on a thick top metal layer. As the coupler provides both *Through* and *Coupled* output ports on the same side for convenient connections with the circuitry and the antenna, it results in an inherent layout asymmetry of its *In/Out* areas. This asymmetry was numerically optimized to minimize differences in performance seen from LHCP and RHCP input ports. The coupler shows a loss of 1 dB.

2) DP Slot Radiator: The main slot radiator is driven differentially from two orthogonal pairs of sectorial patch probes P1–P2 and P3–P4, creating a virtual RF short along the center plane aligned with the complementary pair [32], [33]. Any asymmetry in the differential drive altogether with an insufficient match at the antenna internal input ports connected to the coupler outputs may result in a degradation of the inherent coupler isolation and the IQ balance and lead to a direct cross-coupling between two transmission paths within the antenna aperture, thus calling for accurate codesign between both components. To prevent that, a maximum layout symmetry between two antennas transmit paths should be provided. A 680-μm-long routing was added due to a dimensional mismatch between the coupler and the far ends of the slot circumference. This routing further includes two tapered compact GCPS-to-microstrip transitions ("grounded coplanar wave (GCPW)-to-μ strip Converter" in Fig. 7) and a crossing point between two antenna feed paths. Some additional dummy crossings ("Compensated Cross") were inserted into the complementary feed paths for concurrent optimization with an electromagnetic (EM) solver to minimize this unavoidable layout asymmetry.

3) Complete Antenna on Silicon Half-Space: The major simulation results of the complete circularly polarized antenna (slot radiator with coupler) on a silicon half-space for 210–310 GHz indicate a broadband match better than −26 dB for both LHCP and RHCP input driving ports with the RHCP-to-LHCP port isolation below −22 dB. An AR at boresight for both circular polarizations stays below 1.3. The E-field distribution in the BEOL stack around the slot radiator excited in RHCP polarization at 240 GHz for one arbitrary chosen excitation phase and another one advancing the previous by 90° is plotted in Fig. 7 for completeness, indicating the E-field vector rotation characteristic for circular polarization. The simulated radiation efficiency into a silicon half-space decreases from 51% to 43% and is largely defined by the coupler and feed line losses. An inherent radiation efficiency of the slot radiator is around 90% [32], [33]. The simulations were conducted assuming 2.0×10^7 S/m, 0.02, and 50 $\Omega \cdot$ cm for metal conductivity, the dielectric loss tangent of the BEOL stack, and the silicon bulk resistivity, respectively.

4) Complete Antenna With Silicon Lens: According to the packaging scheme from Section III-B, the primary on-chip antenna system was combined with a high-resistivity hyperhemispherical 9-mm-diameter and 1.25-mm-extension [60] silicon lens. In the current implementation, no matching cap is applied to the lens aperture. For the RX module, the main consequence is limited to an increase in its NF. However, the influence of a missing cap may become more complicated for the TX module. In particular, the rays reflected an odd number of times at the lens–air aperture are prone to polarization change between LHCP and the RHCP and, therefore, can be coupled back to the antenna feed port of the adjacent polarization and is finally retransmitted. The rays undergo an even number of reflections preserve their original polarization

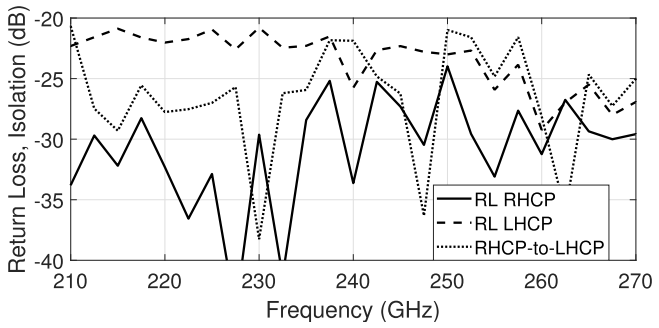

Fig. 9. Full-wave simulated return loss at both RHCP and LHCP driving ports and the isolation between them for the complete chip-on-lens packaged assembly in the transmit mode of operation.

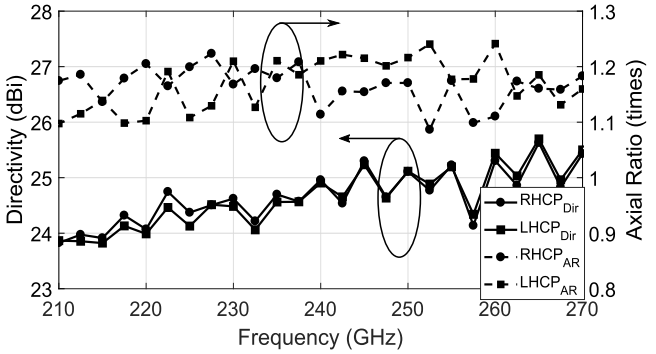

Fig. 10. Full-wave simulated frequency-dependent directivity and AR at boresight for the complete chip-on-lens packaged assembly operated in the transmit mode from the RHCP and LHCP driving ports.

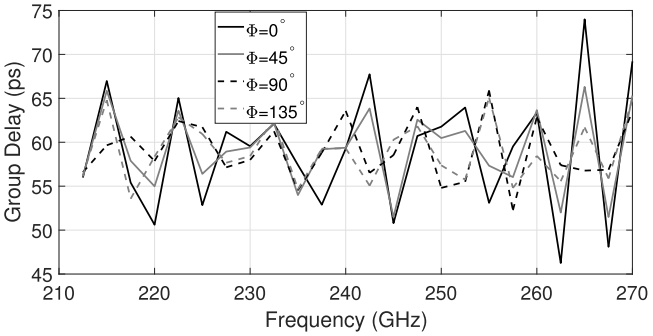

Fig. 11. Full-wave simulated group delay between the LHCP driving port and free space for the complete chip-on-lens assembly. A group delay for different locations in the main beam, including boresight and beam edges defined by a 10-dB taper, is indicated. Four characteristic beam cross sections defined with respect to the coordinate system from Fig. 7 are plotted.

but may lead to group delay distortion if they contribute to the main radiation lobe. Both phenomena are a complex function of wave propagation through the primary-feed on-chip antenna, its illumination pattern of the lens aperture, and ray propagation within the lens volume [61], [62] and were considered in the design process.

A complete chip-on-lens assembly mimicking the packaging scheme from Section III-B was modeled and simulated (Ansoft HFSS) to investigate the influence of internal reflections at the lens–air interface in the transmit mode of operation on key parameters relevant for the implemented polarization-diversity MIMO system. As shown in Fig. 9, both the simulated input match for RHCP and LHCP driving ports as well as isolation between them are superior to -21 dB in the entire 210–270-GHz operation frequency range. The simulated directivity, shown in Fig. 10, ranges between 23.8 and 25.4 dB and is similar for both LHCP and RHCP polarizations. The frequency-dependent AR at boresight (see Fig. 10) for both polarizations stays in the range of 1.08–1.24 and, according to (1), should be sufficient to support a 16-QAM modulation format in the absence of other system impairments. The AR was additionally verified to stay largely below 2 within the entire main beam defined by a 10-dB taper from boresight.

The frequency dependence of a group delay incurred between the RHCP/LHCP driving ports and free space was further simulated for different locations in the main beam. Some selected results for LHCP polarization at boresight and around the beam edges ("10-dB taper") across four characteristic beam cross sections defined with respect to the coordinate system from Fig. 7 are presented in Fig. 11. An average delay of around 60 ps with a typical deviation below 6 ps at boresight and slightly higher at the beam edges is preserved for 210–270 GHz, correlating well with the time of flight through the lens. The periodic-like changes in the deembedded delay should be attributed to the lens internal reflections but may also be partly accounted for by finite accuracy of the meshed volume and the absorbing boundary conditions.

IV. RF Characterization

Two different groups of RF measurements have been performed. The first encompasses a set of single-tone measurements allowing separate investigation of the frequency-dependent lower and upper sideband characteristics for key TX/RX performance metrics. In the second, the measurements involve a combined operation of the TX and RX modules configured into a free-space back-to-back line-of-sight setup. Here, both double-sideband quadrature upconversion and downconversion are performed between the BB TX inputs and the RX outputs, which supports a study of the influence of different hardware imperfections acting simultaneously in the setup mimicking a real wireless link. All measurements have been taken in free space and at the board level, including the influence of all onboard and on-chip components cascaded between the onboard high-speed connector and the lens-coupled on-chip antenna. An absorbing material was applied to cover the major reflecting surfaces to minimize the influence of parasitic reflections in the measurement setup.

A. Single-Tone RF Measurements of TX/RX

Each polarization path (RHCP and LHCP) for both TX and RX modules was characterized independently with a WR-03 (220–325 GHz) frequency extension module from OML, whose output power in the transmit mode and CG in the receive mode was first calibrated for further measurements. The OML module was placed in the antenna far-field zone (30 cm), and all key TX and RX parameters were derived

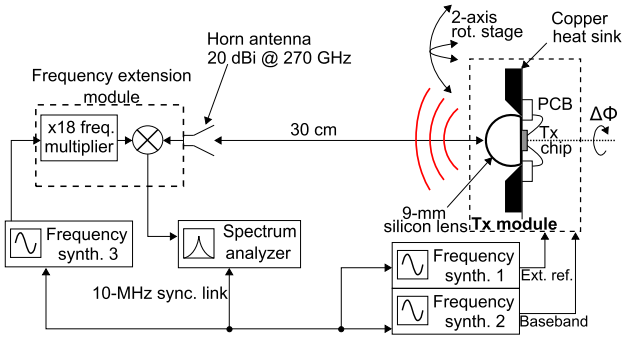

Fig. 12. Free-space measurement setup for single-tone RF characterization in the transmit mode of operation.

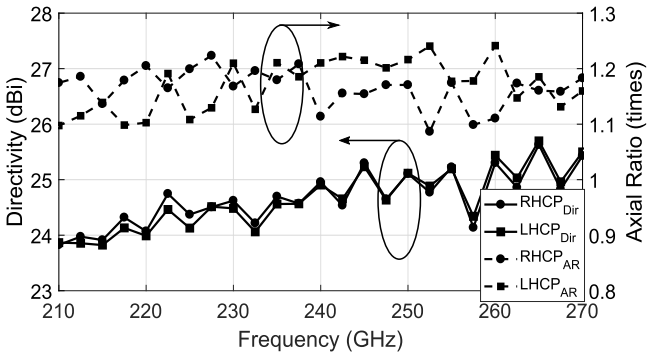

Fig. 13. Measured frequency-dependent AR at boresight and directivity for the TX and RX modules operating with the RHCP polarization.

by applying the Friis transmission equation, which involves the antenna directivity on both sides of the measurement setup. The OML module was equipped with a reference WR-3.4 linearly polarized conical-horn antenna with a 20-dBi directivity at 270 GHz. The antenna was assumed to be an ideal lossless aperture with the square frequency dependence of its directivity for other frequency points. The linearly polarized horn antenna of the OML module captures only a linear projection of the circularly polarized electrical fields generated by the on-chip antennas. Therefore, the complete TX/RX RF characteristics were found by the superposition of two constitutive series of measurements for two relative azimuthal orientations around boresight between TX/RX and OML modules that correspond to the major and the minor axis of a general polarization ellipse [52]. The appropriate free-space measurement setup for the transmit mode of operation is shown in Fig. 12. A complimentary setup was applied for RX measurements with the spectrum analyzer used to acquire signals at the RX BB outputs.

1) Antenna Measurements: A set of antenna measurements, including AR at boresight and copolarization radiation patterns with the corresponding antenna directivity, was performed for both TX and RX modules and each polarization path. Each of the modules was mounted on a motorized 2-D rotational stage with an additional rotational alignment in the azimuthal plane around the boresight, as shown in Fig. 12. Here, by continuous rotation around the boresight, the minor and major axes of the polarization ellipse with respect to the OML module orientation corresponding to the minimum and maximum measured power levels can be found. From the square-root ratio of these power levels, the AR can be calculated [51], [52]. As presented in Fig. 13, an AR of 1.05–1.31 for RHCP polarization was measured for both TX and RX modules in the frequency range of 210–270 GHz. Some differences between both curves can be partly accounted for by a finite alignment accuracy in the measurement setup and insufficient precision of the chip-on-lens assembly. Similar values were acquired for orthogonal LHCP polarization with a maximum deviation between each other below 0.1 and an upper bound of 1.4, correlating well with the simulation results from Fig. 10.

Next, the antenna radiation pattern measurements for both polarization states (RHCP and LHCP) of the TX/RX modules were performed for two previously defined orthogonal

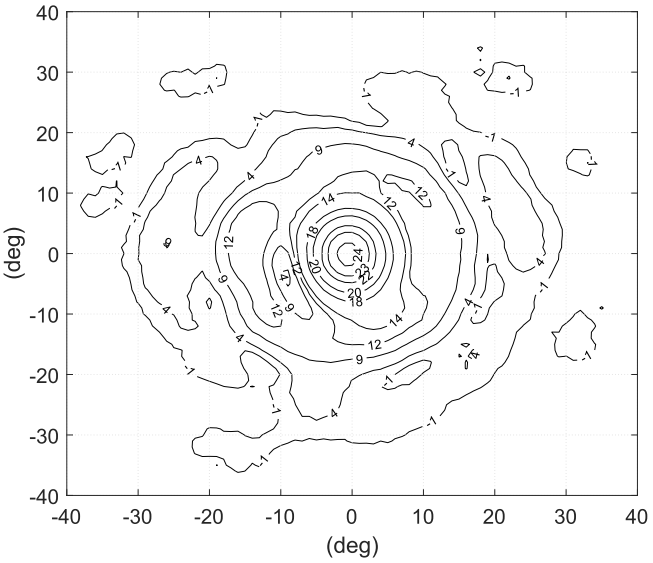

Fig. 14. Measured 2-D contour plot of the copolar RHCP radiation pattern at 240 GHz for the TX module.

orientations corresponding to the major and minor axis of the polarization ellipse in each case, and each total copolar radiation pattern was found by superposition of two constitutive partial measurements. The directivity was finally calculated by integrating the measured values of the 2-D power density copolar patterns acquired over a $\pm 40° \times \pm 40°$ sector of the hemisphere because of the mechanical limitations. The measured frequency-dependent antenna directivity for RHCP polarization, as shown in Fig. 13, increases monotonically from 23.5 to 25.2 dBi in the frequency range of 210—270 GHz for both TX and RX modules, well correlating to the simulation results from Fig. 10. The corresponding LHCP antenna directivity, although not shown, deviates by no more than 0.5 dB from the plotted RHCP values. An azimuthal view of the exemplary chosen RHCP radiation pattern measured at 240 GHz in the transmit mode is shown in Fig. 14, indicating a good beam rotational symmetry.

2) Upconversion Path of TX Module: Two upconversion paths of the TX chip were measured with a tunable 220–255-GHz LO frequency and, for BB signals, up to 20 GHz provided from the board level. As explained in

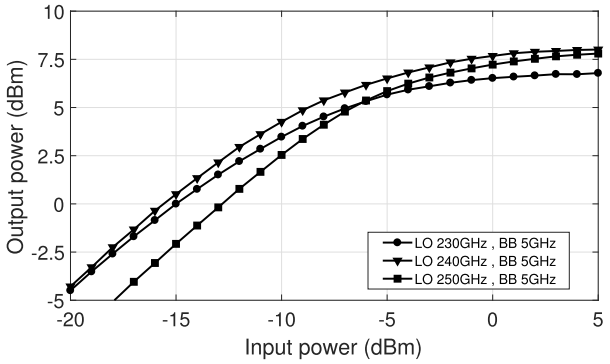

Fig. 15. Measured linearity of the TX RHCP path for different combinations of LO frequencies with an IF frequency of 5 GHz under the simultaneous operation of I and Q channels driven in quadrature at the BB ports for the LSB operation.

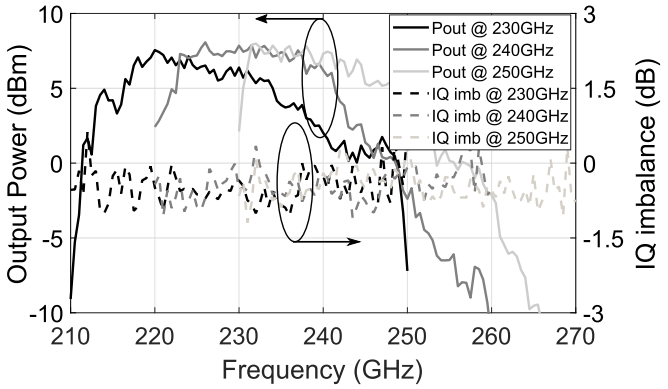

Fig. 16. Measured total radiated power and IQ amplitude imbalance in the RHCP TX path for different LO frequencies and an input power level of −5 dBm at each of the BB driving ports.

Section III-A, the BB input ports were operated single-ended. For characterization of the IQ amplitude imbalance, the I and Q ports were driven separately, whereas, for the total radiated power measurement in the USB and LSB, a broadband (0.5–20 GHz) 90° hybrid (QH0226 Marki) was used to combine the I and Q signals at the mixer BB ports. The TX linearity was further acquired for different combinations of LO and IF frequencies. The LSB linearities of the RHCP path for one arbitrary chosen BB frequency of 5 GHz and three different LO frequencies are shown in Fig. 15, whereas the TX RF characteristics for an input power level of −5 dBm at each of the BB driving ports are gathered in Fig. 16. This power level allows the TX to operate close to saturation and maximizes the link budget for QPSK modulation. According to the discussion from Section III-A, the key TX parameters do not only depend on LO frequency but also vary as a function of the frequency difference between RF and LO, with the LSB typically outperforming USB. The peak radiated power is around 7.5 dBm per polarization channel. The LHCP transmission path exhibits very similar characteristics with a maximum deviation in the radiated power between LHCP and RHCP below 0.5 dB across the measured operation frequency range. An IQ amplitude imbalance was measured below 1 dB in the entire BB BW and is partly defined by the board-level mismatch between I and Q paths incurred by the finite assembly tolerances.

3) Downconversion Path of RX Module: Similar to the TX chip, the Rx BB outputs were operated single-ended, immediately degrading the measured RX power CG by 3 dB. As explained in Section V, the RX BB outputs in the wireless link setup require to be cascaded with the broadband amplifiers (PSPL5882) from Tektronix to raise the output noise spectral density above the noise floor of the consecutive high-speed oscilloscope with an in-build demodulator. This complete cascaded configuration of the RX was further applied in the measurement setup to facilitate a direct comparison of the TX/RX chipset operating in a wireless back-to-back loop with the single-tone RF characterization results. The measured cascaded CG, single sideband (SSB) NF, and IQ amplitude imbalance for the RHCP receive path operated at

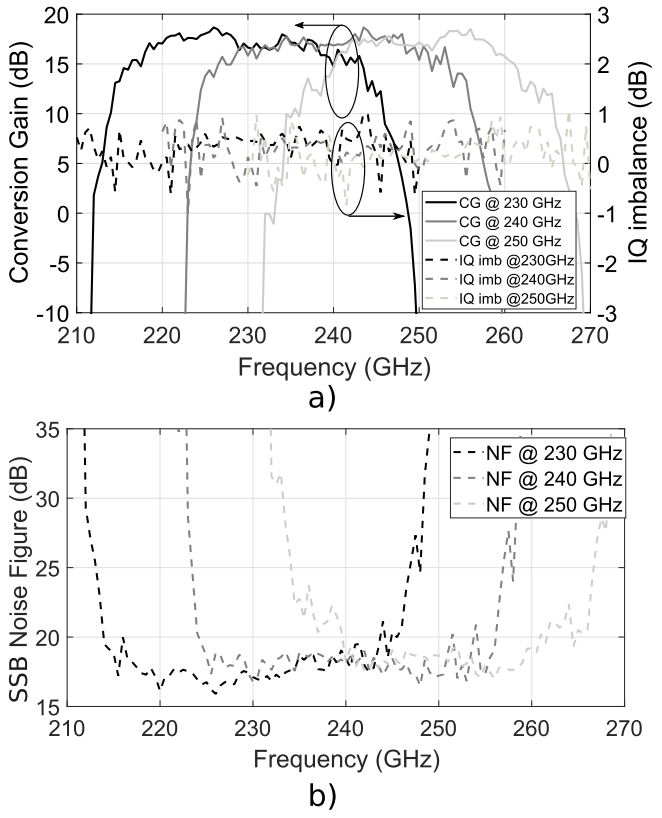

Fig. 17. Measured frequency-dependent (a) CG, (b) IQ amplitude imbalance, and (c) SSB NF in the RHCP RX path for different LO frequencies.

three different LO frequencies are gathered in Fig. 17. The RX shows a peak CG of around 18 dB and a board-level limited 3-dB RF BW of 28 GHz with a very weak dependence on LO frequency. The IQ amplitude imbalance stays below 1 dB, similar to the TX chip. The cascaded in-band SSB NF is around 18 dB and was estimated by employing an indirect measurement method from [63] due to the lack of a noise source at these frequencies in our lab. According to this method, the NF can be calculated from the measured CG and noise power spectral density, N_{out}, at the RX output as

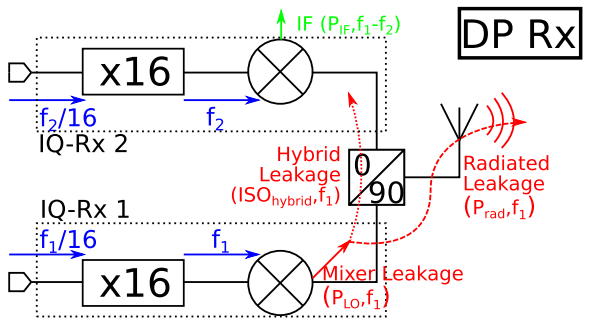

Fig. 18. Simplified block diagram of the RX chip in a test configuration applied to measure the isolation between two driving ports of the antenna system.

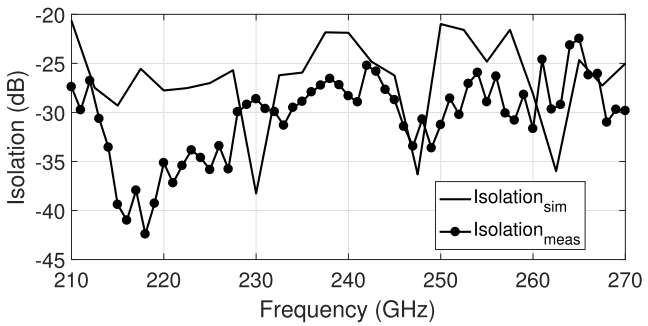

Fig. 19. Measured and simulated isolation between two driving ports (RHCP and LHCP) of the antenna system.

follows:

$$\mathrm{NF} = \frac{\mathrm{SNR_{in}}}{\mathrm{SNR_{out}}} = \frac{N_{\mathrm{out}}}{N_{\mathrm{in}} \times \mathrm{CG}} \tag{2}$$

under the assumption of only thermal noise power spectral density, $\mathrm{N_{in}}$, present at the RX input (-174 dBm/Hz at 298 K). The measurement results for the complementary LHCP path (not shown for clarity) deviate by no more than 0.5 dB from the plotted RHCP characteristics.

4) LO Path of TX/RX Modules: According to the discussion from Section III-A, the nonideal LO generation path is a source of: 1) direct leakage between the externally provided LO driving frequency (LO/16) and the RX BB outputs; 2) insufficient isolation through the upconversion/downconversion mixer to the RF (antenna) port; and 3) harmonic spurs in a single ($\times$15 and $\times$17) and twofold ($\times$14 and $\times$18) spectral distance to the main LO ($\times$16) tone. The first from the list was measured at -50 to -55 dB below the power level of the tunable 13.75–16.25-GHz external LO driving signal, whereas the LO leakage through the mixer blocks was typically at a -20-dBc level. A suppression level of the parasitically upconverted/downconverted BB signals as referred to the wanted $\times$16 mixing products was characterized across the 220–260-GHz LO tuning range. For 225–245 GHz, the suppression was better than 30–45 dB, but it dropped to around 15–20 dB for other LO frequencies.

The close-proximity phase noise of the TX LO path driven from the reference Keysight E8257D synthesizer (see Section III-A) was measured after downconversion with an OML extension module and was found to scale as expected according to 20 $\log_{10}(16) = 24.1$ dB.

5) On-Chip Isolation Between Two Polarization Paths: As discussed in Sections II and III-C, direct leakage between two antenna driving ports on each chip, as shown in Figs. 1 and 7, is one of two major sources of potential coupling between two orthogonal data streams. A dedicated test procedure was developed to facilitate the measurement of this leakage, which is outlined in Fig. 18 for the RX chip. The setup exploits the presence of two independent LO paths, IQ-RX 1 and IQ-RX 2, operating at two different LO frequencies, f_1 and f_2, with a frequency offset $f_1 - f_2$. Here, the LO power, P_{LO}, leaking through the downconversion mixer, IQ-RX 1, can be downconverted to P_{IF} by the second mixer, IQ-RX 2, due to the finite isolation between two ports of the antenna system, denoted as $\mathrm{ISO_{Hybrid}}$. $\mathrm{ISO_{Hybrid}}$ can be calculated as

$$\mathrm{ISO_{Hybrid}(dB)} = P_{\mathrm{IF}} - P_{\mathrm{rad}} - \mathrm{CG_{IQ-RX2}} - 2 \cdot \mathrm{Ant_{Loss}} \tag{3}$$

where $\mathrm{CG_{IQ-RX2}}$ denotes the previously measured CG of the IQ-RX 2 RX path and $\mathrm{Ant_{Loss}}$ refers to the simulated loss of the complete antenna system from Section III-C. P_{rad} is the LO power leaking through the mixer IQ-RX 1 corrected by the insertion loss incurred by the antenna system, as $P_{\mathrm{rad}} = P_{\mathrm{LO}} - \mathrm{Ant_{Loss}}$, and was characterized directly with the free-space single-tone measurement setup from Fig. 12. The isolation was measured in the 210–270-GHz frequency range by simultaneous tuning in both LO paths with a constant frequency offset of 500 MHz and is presented Fig. 19 altogether with the previous simulation results from Fig. 9, both correlating well with each other. The isolation is superior to -22 dB for the entire 210–270-GHz range and is, therefore, expected to be less critical than that incurred by the AR.

A similar setup cannot be applied to the TX chip because of the reverse isolation of the PA block inserted between the upconversion mixer and the antenna system. Therefore, it assumed that both RX and TX chips show similar on-chip isolation between RHCP and LHCP paths due to identical antenna layout.

B. TX/RX RF Measurements in a Back-to-Back Loop

The effective channel BW of each complete transmission path (LHCP or RHCP) in a back-to-back configuration is set by RF bandpass and BB LP characteristics of both TX and RX modules acting together by performing the combined double-sideband upconversion and downconversion between the corresponding BB TX and RX ports. In particular, double sideband operation involves the asymmetry between LSB and USB of both modules in the transmission process, and therefore, the frequency-dependent characteristics, both amplitude and group delay, of the complete path are not simple replicas of the TX and RX RF properties found from single-tone measurements. The aggregate isolation between both transmission paths is related to a direct leakage between the RHCP and LHCP antenna driving ports on each chip, the antenna axial-ratio on both sides of the link, and a relative azimuthal orientation around boresight between the transmit and the

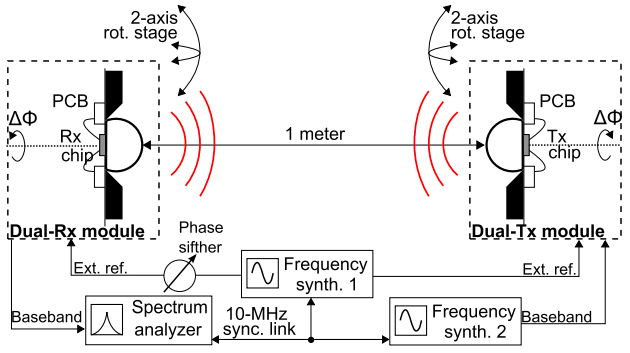

Fig. 20. Measurement setup for characterization of the TX/RX in a back-to-back configuration.

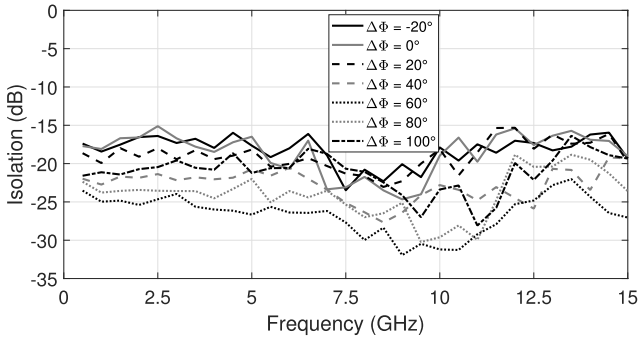

Fig. 21. Measured isolation between the TX RHCP path and the RX LHCP path at a 1-m distance as a function of the BB frequency for different relative azimuthal orientations between the TX and the RX operating at 230 GHz.

receive block. The highest cross-polarization incurred coupling appears when the major axes of the polarization ellipse on both TX and RX side are rotated by around 90° and corresponds to the sum of the antenna XPD, on both sides.

In order to measure the TX/RX performance in a back-to-back configuration, the following setup, as shown in Fig. 20, was used. Here, the TX and RX modules were placed in the line-of-sight at a 1-m distance, and all on-chip LO generation paths were driven from a single frequency synthesizer. The LO frequency was tuned between 210 and 270 GHz with the corresponding BB sweep of 15 GHz for each LO frequency settings. Although the isolation between RHCP and LHCP paths does not depend on a relative phase difference between the TX and RX LO chains to the first-order extend, a phase shifter, as shown in Fig. 20, was used to facilitate the channel measurements for both of them by ensuring the maximum power transfer for each of the consecutive I and Q paths in each orthogonal polarization.

An exemplary chosen measured isolation between the TX RHCP path and the RX LHCP path as a function of BB frequency for different relative azimuthal orientations between TX and RX operating at 230 GHz is shown in Fig. 21. The measurement results for the opposite combination (TX-LHCP-to-RX-RHCP), although not shown, are very similar. Please note that the measured aggregated isolation includes not only the influence of the expected antenna XPD and direct leakage between two antenna driving ports

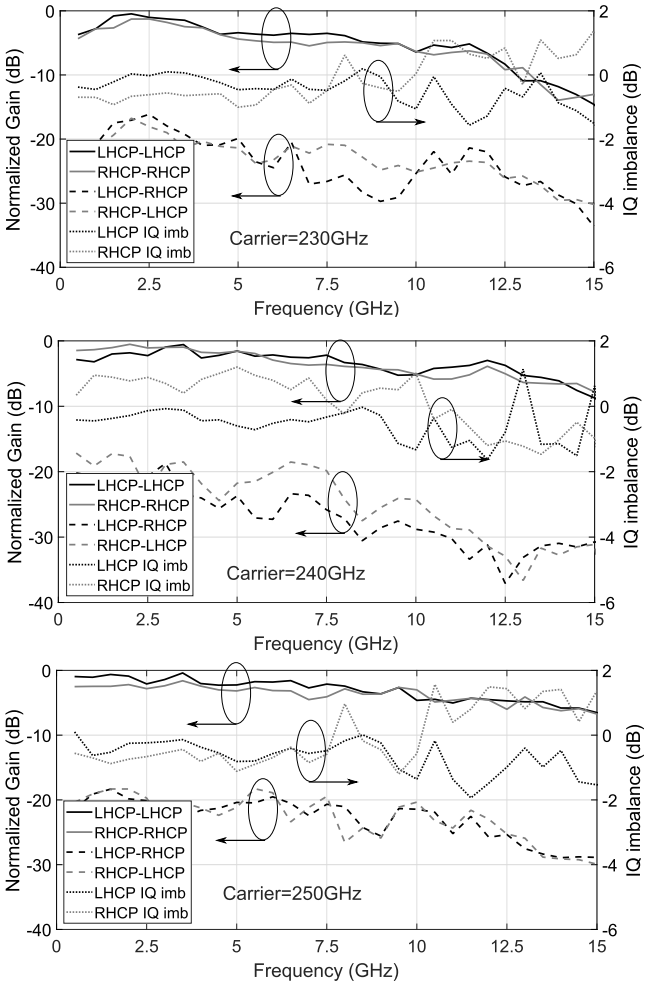

Fig. 22. Channel BW, IQ amplitude imbalance, and isolation between the RHCP and LHCP transmission paths for different carrier frequencies and the worst case azimuthal alignment between the TX and RX modules at a 1-m distance. Each of the plots is normalized to its corresponding maximum signal level at the RX output.

on each chip but it is also affected by the finite alignment accuracy and the presence of standing waves between both modules. For the worst case alignment corresponding to angle $\Delta\Phi$ of around 80–100°, the isolation varies between −17 and −18 dB across the entire BB BW, thus correlating well with the previous single-tone measurements from Section IV-A and simulation results from Section III-C that predict the antenna XPD of 18–32 dB and the antenna on-chip isolation between the RHCP and LHCP driving ports of −40 to −22 dB across 210–270 GHz. According to [56], such isolation should be sufficient for 16-QAM simultaneous operation of both polarization paths in the absence of other link impairments. The next set of plots in Fig. 22 presents the isolation measured for three different LO frequencies under the worst case alignment scenario, indicating very consistent values with low dependence on the LO frequency. The 6-dB defined BB channel BW is above 13.5 GHz for all LO frequencies with a typical in-band IQ amplitude imbalance below 1 dB. The amplitude imbalance grows up to 2 dB for some frequency points in the higher end of the BB BW and

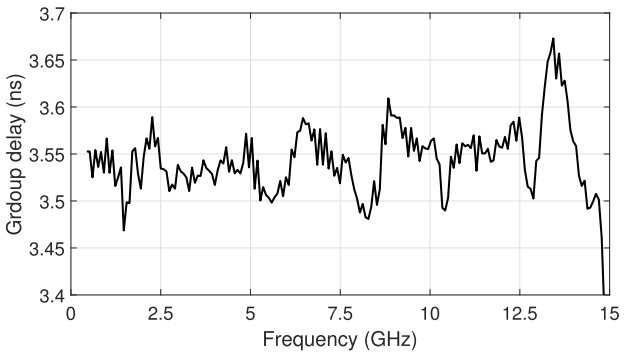

Fig. 23. Measured group delay through a 1-m distance line-of-sight link across the entire 15-GHz BB BW for the I channel of the RHCP transmission path operating at 230 GHz.

is largely attributed to a finite control of the board-level LP filter characteristics from Fig. 6.

The group delay of the entire 1-m distance wireless setup in a back-to-back configuration was measured by connecting a two-port vector network analyzer (VNA) to the IQ BB ports of the TX and RX modules for each separate polarization. An arbitrarily chosen group delay plot across the entire 15-GHz BB BW for the I channel of the RHCP transmission path operating at 230 GHz is shown in Fig. 23. The measured delay of 3.55 ns with a typical in-band variation below $\pm$50 ps in the entire operating BW corresponds well to a total propagation time through the air path, onboard filters, and lens-coupled antennas on both sides of the link. Although the group delay measurements involving a very large number of periods in the transmission path challenge the measurement accuracy (800 for a carrier frequency of 240 GHz at a 1-m distance), the LO frequency-independent location and shape of the ripples in the plot correlate with the ones of the onboard filter, as shown in Fig. 6 and in [40], indicating that the group delay dispersion is largely dominated by the packaging and not by RF bandpass response of the on-chip circuitry. The in-band group delay variation (below 13 GHz) has two main sources: first, the combination of the on-chip circuitry with the onboard filter. Only in the RX side, this adds a waviness of 10 ps as it was reported in [40]. Second, although the setup was cover by absorbers, it is not possible to eliminate the standing waves present in the 1-m wireless link. This effect increases the waviness of the in-band group delay. On the other side, the absolute maximum at 13 GHz shows a variation of 100 ps over the average group delay of 3.55 ns, which correlates well with the variation expected after cascading the two onboard filters present in the wireless link (TX and RX). A $\pm$50-ps in-band variation is comparable to a symbol duration for the highest modulation speed reported here and, therefore, requires some linear equalizer to be applied in the communication setup.

V. Wireless Communication Link

A. Measurement Setup Description

For simultaneous wireless measurements of RHCP and LHCP transmission paths in a line-of-sight 1-m distance configuration, two two-channel 100-Gs/s Tektronix DPS77004SX real-time oscilloscopes with single-ended input ports and four 50-Gs/s Tektronix AWG70001A arbitrary-waveform generators (AWGs), synchronized in pairs, were used. A set of phase-matched cables was applied to connect the TX and RX onboard BB connectors to the corresponding ports of the generators and oscilloscopes. Due to the low noise level at the RX outputs, a set of broadband amplifiers PSPL5882 from Tektronix was placed between the RX output and the oscilloscope inputs. This was done to amplify the signal power and the noise power spectral density at the output of the RX above the oscilloscope noise floor to shield the effect of the latter from the wireless communication link results. The PSPSL5882 amplifiers have a gain of 16 dB over a 35-GHz BW and an NF of 6 dB measured at 1.5 GHz. As explained in Sections III-A and IV-A, the differential input and output BB stages of the RX and TX needed to be operated as single-ended, resulting not only in an SNR decrease but more important in a degraded drive balance leading to a more pronounced frequency dispersion in the operation BW and a higher leakage between the I and Q paths. The received digitized data in the oscilloscope were evaluated with a vector signal analysis (VSA) software, which provides an adaptive decision-directed FIR feed-forward equalizer for linear distortion compensation operating together with the carrier/clock synchronization loop.

TABLE I
QPSK Waveform Parameters at the AWG Output

QPSK data-rate	P_{out} (dBm)	90% BW (GHz)	First-zero BW (GHz)	EVM_{rms} (%)
20 Gb/s	-2.1	5.5	8.5	1.8
30 Gb/s	-2.8	8.2	12.75	2
40 Gb/s	-4	10.7	17	3
50 Gb/s	-7.7	13.25	21.75	4
55 Gb/s	-9.6	14.5	23.5	6

For the highest quality of the modulated waveforms driving the TX ports, the AWG nonideal frequency response was first compensated by predistortion. To reduce a spectral spread of the modulated waveforms to fit into the limited BW of the generators and TX/RX modules, the pulse-shaping with a root-raised cosine filter (RRC) (roll-off factor of 0.2–0.7) was further applied, and the AWG waveform quality was finally determined with the VSA software of the oscilloscopes. Table I gathers the measured waveform parameters for QPSK speeds ranging from 20 to 55 Gb/s. The parameters include EVM for pseudo random bit sequence (PRBS) 9 data sequence, combined power for I and Q outputs, 90% power containment BW, and full BW defined by the first zero-crossing. By comparison with Fig. 15, it can be noticed that above 40 Gb/s, the generators do not provide sufficient output power for full compression of the TX module, which may lead to additional changes in the frequency-dependent channel response. Next, the EVM values grow to around 6% toward 55 Gb/s and, thus, contribute to an EVM increase of the total back-to-back 1-m link. A 90% power BW for 50-Gb/s QPSK roughly matches that of the measured channel BB BW.

A block diagram of the complete measurement setup is shown in Fig. 24. The relative azimuthal orientation between

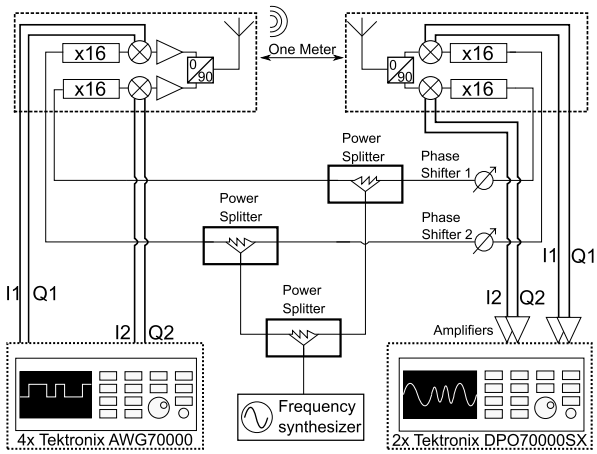

Fig. 24. Block diagram of the wireless link setup.

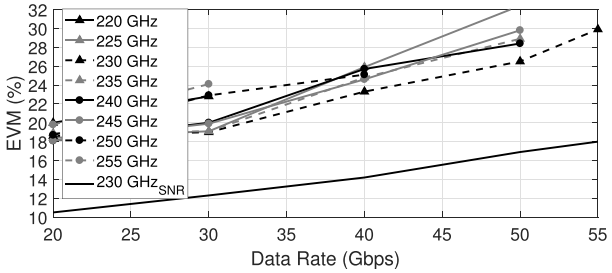

Fig. 25. Measured EVM for the QPSK-modulated RHCP transmission path as a function of modulation speed and carrier frequency. The expected EVM from the measured SNR at 230 GHz is given for comparison.

the TX and RX modules was chosen to correspond to the highest leakage between the RHCP and LHCP paths, as found from the previous single-tone measurements in a back-to-back configuration (see Section IV-B). Both transmission channels were operated simultaneously at the same carrier frequency to double the spectral efficiency of the MIMO link. Therefore, the external LO driving frequency was provided from the same synthesizer after the power split. A set of phase shifters was also inserted to expedite the carrier synchronization for each independent transmission path, particularly in the presence of low SNR at the RX outputs for the highest modulation speeds. An adaptive decision-directed FIR feed-forward equalizer with a varying number of taps of up to 61 was applied to the received signals [64].

B. Single-Polarization Single-In Single-Out (SISO) Measurement

To separate the EVM contributions resulting from finite isolation between the RHCP and LHCP transmission paths from those related to the hardware impairments in each individual MIMO path, the link was first characterized under the single-path operation conditions and for multiple carrier frequencies between 220 and 255 GHz.

The measured EVM for the arbitrary chosen QPSK-modulated RHCP path as a function of the modulation speed and the carrier frequency is shown in Fig. 25. A maximum data rate of 55 Gb/s with an EVM of 30% was

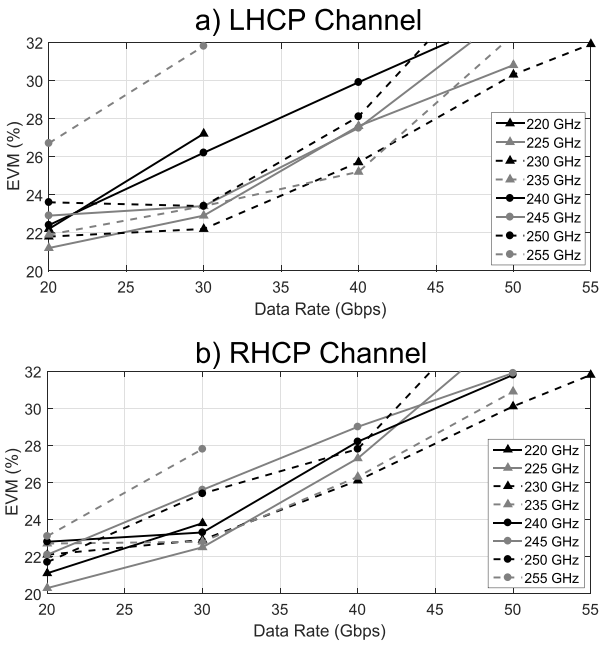

Fig. 26. Measured EVM for the QPSK-modulated (a) LHCP and (b) RHCP transmission paths under simultaneous operation as a function of modulation speed and carrier frequency. A comparison with the expected EVM from the measured.

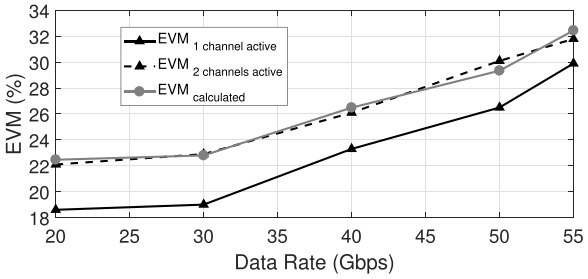

Fig. 27. Measured and calculated EVM for the QPSK-modulated RHCP and LHCP transmission paths under simultaneous operation as a function of modulation speed and carrier frequency.

achieved at 230 GHz, where the entire available BB BW was fully exploited and the aggregate influence of all single-path related hardware imperfections acting simultaneously was minimized. For 225–245 GHz, the measured EVM dependence on LO frequency and modulation speed shows a similar trend up to 50 Gb/s with relatively minor variation between all curves. This variation is determined mainly by differences in: 1) the transmitted output power; 2) the TX asymmetry between LSB and USB; and 3) the suppression level of the externally provided LO driving tone (LO/16) at the RX BB outputs with respect to the downconverted power density of the modulated spectrum. For sufficiently low modulation speeds, the leaking LO/16 tone can be practically eliminated with the applied RRC filter at the RX output, but this filtering can no longer be applied without affecting the modulated spectrum for the higher modulation BW reaching the spectral location of the LO/16 tone. For LO frequencies outside of the 225–245-GHz range, the EVM grows faster, and it is mainly a direct consequence of the insufficient suppression of the $\times 15$ and $\times 17$ harmonic spurs in the LO

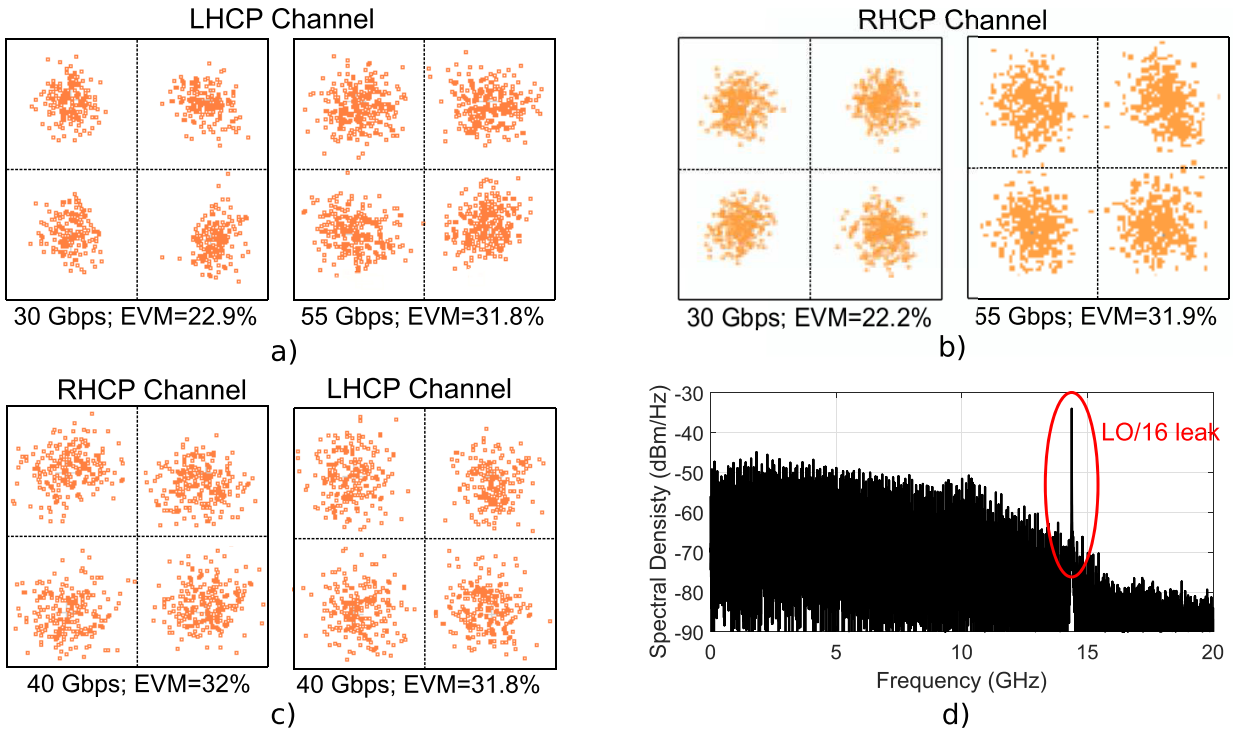

Fig. 28. Set of the measured constellation diagrams with one arbitrary chosen downconverted spectrum before demodulation. (a) 30- and 55-Gb/s LHCP paths at 230 GHz and 1-m distance. (b) 30- and 55-Gb/s RHCP paths at 230 GHz and 1-m distance. (c) 40-Gb/s LHCP and RHCP paths at 230 GHz and 2-m distance. (d) Spectral density of the downconverted 55-Gb/s QPSK waveform at the RX RHCP BB ports before demodulation.

generation paths; as discussed in Sections III-A and IV-A. An EVM contribution related to the IQ imbalance in the link was found not to be the major factor of the overall EVM degradation. With the equalizer in the RX path, the phase and amplitude IQ errors determined from the constellation diagrams were typically below 3° and 0.2 dB, respectively, up to around 40 Gb/s.

For a better understanding of the minimum achieved EVM at low data rates, an SNR at the RX outputs before demodulation was measured directly, and the resulting minimum AWGN-limited EVM bound (EVM $= 1/(\mathrm{SNR})^{1/2}$) for 230 GHz is additionally plotted in Fig. 25. A nonnegligible discrepancy between the measured EVM and the calculated minimum bound can be noticed. This minimum value of around 18% holds for the lower wireless distance, indicating that the SNR does not limit the link in its current state. By comparison with our previous wireless experiments [15], [16], [36] that operated the TX/RX BB ports fully differentially and reported an EVM as low as 7% for the same baud rates, the main source of EVM deterioration was found to be an imbalanced single-ended drive of the high-speed ports through the wire-bonded interconnects, as previously mentioned in Section III-A. A minimum EVM of 18% in each single-polarization path currently prevents the MIMO operation with higher order modulation formats, such as 16-QAM, even though the measured RHCP–to–LHCP isolation may potentially provide it.

C. DP MIMO Measurement

Similar plots to those from Fig. 25 were acquired for two transmission paths (RHCP and LHCP) operating simultaneously, as shown in Fig. 26. It can be noticed that both paths show some EVM differences for the same combination of LO frequency and modulation speed, but the general EVM trends for both plots are well preserved. Some differences between the RHCP and LHCP links are attributed mainly to: 1) the limited package-level assembly tolerances; 2) the differences in XPDs for RHCP–to–RHCP and LHCP–to–LHCP polarizations; and 3) the spread of phase error for both LO paths that need to be synchronized simultaneously. The EVM contributions related to the single-channel operation (see Fig. 25) can be combined with the channel-to-channel isolation (see Fig. 22) into an aggregate EVM [56], modeling the polarization leakage as the Gaussian noise. This EVM is additionally plotted in Fig. 27 for the carrier frequency of 230 GHz to allow direct comparison with the directly measured total EVM. As can be noticed, both the calculated (denoted as $\mathrm{EVM}_{\mathrm{calculated}}$) and the measured values correspond well to each other, indicating the absence of other potential link impairments. The maximum aggregate data rate of 110 Gb/s with an EVM of 31.9% was achieved at 230 GHz, similar to the single-polarization operation. Assuming an AWGN channel approximation [56], the corresponding BER should stay below 10^{-3}. At 255 GHz, which is in the operation range of the IEEE 802.15.3d-2017 standard (channels 1, 2, 33, and 49) [1], a maximum data rate of 60 Gb/s was achieved. The standard does not define any specific link distance. However, it requires a postforward-error-correction (FEC) BER better than 10^{-12}. According to [65], any BER better than $4.5 \cdot 10^{-3}$ can be corrected to the level of 10^{-15} applying FEC codes. The results presented here align with the signal quality required by the standard. For a 2-m distance link, the maximum link speed was

TABLE II
STATE-OF-THE-ART OF ELECTRONIC-BASED WIRELESS LINKS ABOVE 200 GHz

Ref.	[10]	[9]	[29]	[21]	[20]	[37]/ [38]/ [39]	[30]	[15]	This Work
Technology	35nm InP	80nm InP	130nm SiGe	40nm CMOS	40nm CMOS	130nm SiGe	130nm SiGe	130nm SiGe	130nm SiGe
Frequency (GHz)	240	270	190	300	265	225-255	240	225-255	225-255
Modulation	8-PSK	16-QAM	BPSK	16-QAM	16-QAM	16/32/64-QAM	BPSK	16-QAM	QPSK
On-chip LO ?	yes	no	no	no	no	yes	yes	yes	yes
Packaging	waveguide	waveguide	-	-	COB	COB	COB	COB	COB
Antenna type	horn	horn	dipole	horn	horn	on-chip ring + lens	double folded dipole + lens	on-chip ring + lens	on-chip slot + lens
Antenna gain (dBi)	-	50	5	-	24	26	14	26	25
Data-rate (Gb/s)	96	100	50	32	80	90/90/81	25	100	100/80
Distance (cm)	40m	222	0.6	1	3	100	100	20	100/200
EVM (%)	21.6	16.5_1	$3{\cdot}10^{-4}{}_2$	16.1	16.3	15/12/8.5	$2.2{\cdot}10^{-4}{}_2$	17	32
P_{DC} (W)	-	-	0.154	2.05	1.79	1.96	1.41	0.95	2.85
Efficiency (pJ/b)	-	-	3_3	65	22.4	$22/11_3$	56.4	$14/5.5_3$	$25.9/12_{3\ 4}$
# of channels	1 IQ channel	1 channel	1 channel	1 channel	1 channel	1 IQ channel	1 channel	1 IQ channel	2 IQ channels

$_1$Measured SNR (dB); $_2$BER; $_3$Without LO generation circuitry; $_4$For a 1-meter distance

reduced to 80 Gb/s and was achieved at 230 GHz with an EVM of 32%. A set of the measured constellation diagrams with one arbitrary chosen spectrum of the downconverted 55 Gb/s QPSK waveform at the RX BB ports before demodulation is presented in Fig. 28. Here, the presence of the external LO/16 driving signal is evident.

The link is not noise-limited; therefore, the effect of further increases in the distance on the link quality cannot be simply extrapolated from the previous measurements. The measured EVM does not scale according to the link-budget calculation defined by the Friss formula, but it is dominated by other effects, such as the asymmetric operation of the differential pairs. However, as explained in Section III-C, the antenna directivity of the modules can be extended by attaching a bigger lens to the chip, allowing for higher link distances holding the performance.

The major measured results for the presented polarization-diversity MIMO system are compared with the current state-of-the-art fully electronic solutions operating above 200 GHz in Table II.

VI. CONCLUSION

In this article, the feasibility of doubling the spectral efficiency of a line-of-sight wireless transmission by applying the polarization-diversity MIMO to a set of highly integrated and fully packaged fundamentally operated direct-conversion IQ TX and RX modules has been demonstrated. Each of the modules is implemented in 0.13 μm SiGe HBT technology as a single-chip solution in combination with a low-cost COB packaging for the high-speed BB signaling and the silicon lens-coupled on-chip antenna interface to free space. The chipset can simultaneously transmit two orthogonal circular polarizations (RHCP and LHCP) without the need of a high-speed depolarizer in the BB for any relative azimuthal orientation between the TX and RX modules, solving the problem of the relative orientation between the TX and the RX. This, in addition to the used QPSK modulation scheme, relaxes the complexity of the future BB circuitry attached to this system. These two points are particularly important steps toward the realization of future mobile applications at this frequency range.

This article further presented a detailed analysis of the major RF hardware imperfections limiting the system-level EVM, which were separated into two different contribution groups related to: 1) the single-channel operation at a time and 2) the on-chip and free-space leakage between two independent channels paths.

On the link level, channel-to-channel isolation of at least 18 dB for the entire measured 210–270 GHz band was achieved, which is sufficient for simultaneous operation of two high data-rate 16-QAM modulated waveforms in the absence of other potential link impairments. In view of a minimum EVM of around 18% achieved for each of the channels operating separately, caused by the single-ended operation of the upconversion and downconversion mixers, the MIMO operation with a 16-QAM modulation format was not possible. For QPSK modulation, a maximum aggregate data rate of 110 and 80 Gb/s was achieved at 230 GHz for 1- and 2-m distances, respectively. For the highest LO frequency of 255 GHz, which is the operating range of the new IEEE 802.15.3d-2017 standard, 60 Gb/s was demonstrated. With some improvements on circuit level in each single-polarization path and in the antenna XPD, considerable improvements in an aggregated date rate beyond 100 Gb/s are anticipated.

ACKNOWLEDGMENT

The authors would like to thank Tektronix for providing a set of two additional AWGs that facilitated the characterization and simultaneous operation of two wireless transmission links.

REFERENCES

[1] *IEEE Standard for High Data Rate Wireless Multi-Media Network–Amendment 2: 100 Gb/s Wireless Switched Point-to-Point Physical Layer*, Standard IEEE Std 802.15.3d-2017 (Amendment to IEEE Std 802.15.3-2016 as amended by IEEE Std 802.15.3e-2017), Oct. 2017, pp. 1–55.

[2] K.-C. Huang and Z. Wang, "Terahertz terabit wireless communication," *IEEE Microw. Mag.*, vol. 12, no. 4, pp. 108–116, Jun. 2011.

[3] J. Federici and L. Moeller, "Review of terahertz and subterahertz wireless communications," *J. Appl. Phys.*, vol. 107, no. 11, Jun. 2010, Art. no. 111101.

[4] H.-J. Song and T. Nagatsuma, "Present and future of terahertz communications," *IEEE Trans. THz Sci. Technol.*, vol. 1, no. 1, pp. 256–263, Sep. 2011.

[5] M. Latva-aho and K. Lepannen, "Key drivers and research challenges for 6G ubiquitous wireless intelligence," 6G Flagship, Oulu, Finland, Tech. Rep., 2019, pp. 1–13.

[6] I. Kallfass *et al.*, "Towards MMIC-based 300GHz indoor wireless communication systems," *IEICE Trans. Electron.*, vol. E98.C, no. 12, pp. 1081–1090, Dec. 2015.

[7] M. Urteaga, Z. Griffith, M. Seo, J. Hacker, and M. J. W. Rodwell, "InP HBT technologies for THz integrated circuits," *Proc. IEEE*, vol. 105, no. 6, pp. 1051–1067, Jun. 2017.

[8] X. Mei *et al.*, "First demonstration of amplification at 1 THz using 25-nm InP high electron mobility transistor process," *IEEE Electron Device Lett.*, vol. 36, no. 4, pp. 327–329, Apr. 2015.

[9] H. Hamada *et al.*, "300-GHz. 100-Gb/s InP-HEMT wireless transceiver using a 300-GHz fundamental mixer," in *IEEE MTT-S Int. Microw. Symp. Dig.*, Jun. 2018, pp. 1480–1483.

[10] F. Boes *et al.*, "Ultra-broadband MMIC-based wireless link at 240 GHz enabled by 64GS/s DAC," in *Proc. 39th Int. Conf. Infr., Millim., THz Waves (IRMMW-THz)*, Sep. 2014.

[11] I. Kallfass *et al.*, "64 Gbit/s transmission over 850 m fixed wireless link at 240 GHz carrier frequency," *J. Infr., Millim., THz Waves*, vol. 36, no. 2, pp. 221–233, Jan. 2015.

[12] I. Kallfass *et al.*, "All active MMIC-based wireless communication at 220 GHz," *IEEE Trans. THz Sci. Technol.*, vol. 1, no. 2, pp. 477–487, Nov. 2011.

[13] H.-J. Song, J.-Y. Kim, K. Ajito, N. Kukutsu, and M. Yaita, "50-Gb/s direct conversion QPSK modulator and demodulator MMICs for terahertz communications at 300 GHz," *IEEE Trans. Microw. Theory Techn.*, vol. 62, no. 3, pp. 600–609, Mar. 2014.

[14] J. Antes *et al.*, "Transmission of an 8-PSK modulated 30 Gbit/s signal using an MMIC-based 240 GHz wireless link," in *IEEE MTT-S Int. Microw. Symp. Dig.*, Jun. 2013, pp. 1–3.

[15] P. Rodriguez-Vázquez, J. Gryb, B. Heinemann, and U. R. Pfeiffer, "A 16-QAM 100 Gbps 1-meter wireless link with an EVM of 17% at 230 GHz in a SiGe technology," *IEEE Microw. Wireless Compon. Let.*, vol. 22, no. 2, pp. 61–63, Feb. 2019.

[16] J. Grzyb, P. R. Vazquez, N. Sarmah, B. Heinemann, and U. R. Pfeiffer, "Performance evaluation of a 220–260 GHz LO tunable BPSK/QPSK wireless link in SiGe HBT technology," in *Proc. 48th Eur. Microw. Conf. (EuMC)*, Sep. 2018, pp. 1397–1400.

[17] S. Lee *et al.*, "Record RF performance of 45-nm SOI CMOS technology," in *IEDM Tech. Dig.*, Dec. 2007, pp. 255–258.

[18] H. Li *et al.*, "Technology scaling and device design for 350 GHz RF performance in a 45nm bulk CMOS process," in *Proc. IEEE Symp. VLSI Technol.*, Jun. 2007, pp. 56–57.

[19] J.-D. Park, S. Kang, S. V. Thyagarajan, E. Alon, and A. M. Niknejad, "A 260 GHz fully integrated CMOS transceiver for wireless chip-to-chip communication," in *Proc. Symp. VLSI Circuits (VLSIC)*, Jun. 2012, pp. 48–49.

[20] S. Lee *et al.*, "9.5 an 80Gb/s 300GHz-band single-chip CMOS transceiver," in *IEEE ISSCC Dig. Tech. Papers*, Feb. 2019, pp. 170–172.

[21] S. Hara *et al.*, "A 32Gbit/s 16QAM CMOS receiver in 300GHz band," in *IEEE MTT-S Int. Microw. Symp. Dig.*, Jun. 2017, pp. 1703–1706.

[22] K. Takano *et al.*, "17.9 a 105Gb/s 300GHz CMOS transmitter," in *IEEE ISSCC Dig. Tech. Papers*, Feb. 2017, pp. 308–309.

[23] S. V. Thyagarajan, S. Kang, and A. M. Niknejad, "A 240 GHz fully integrated wideband QPSK receiver in 65 nm CMOS," *IEEE J. Solid-State Circuits*, vol. 50, no. 10, pp. 2268–2280, Oct. 2015.

[24] S. Kang, S. V. Thyagarajan, and A. M. Niknejad, "A 240 GHz fully integrated wideband QPSK transmitter in 65 nm CMOS," *IEEE J. Solid-State Circuits*, vol. 50, no. 10, pp. 2256–2267, Oct. 2015.

[25] P. Hillger, J. Grzyb, R. Jain, and U. R. Pfeiffer, "Terahertz imaging and sensing applications with silicon-based technologies," *IEEE Trans. THz Sci. Technol.*, vol. 9, no. 1, pp. 1–19, Jan. 2019.

[26] B. Heinemann *et al.*, "SiGe HBT with fx/fmax of 505 GHz/720 GHz," in *IEDM Tech. Dig.*, Dec. 2016, pp. 1–3.

[27] M. Schroter *et al.*, "The EU DOTSEVEN project: Overview and results," in *Proc. IEEE Compound Semiconductor Integr. Circuit Symp. (CSICS)*, Oct. 2016, pp. 1–4.

[28] C. Jiang, A. Cathelin, and E. Afshari, "A high-speed efficient 220-GHz spatial-orthogonal ASK transmitter in 130-nm SiGe BiCMOS," *IEEE J. Solid-State Circuits*, vol. 52, no. 9, pp. 2321–2334, Sep. 2017.

[29] D. Fritsche, P. Starke, C. Carta, and F. Ellinger, "A low-power SiGe BiCMOS 190-GHz transceiver chipset with demonstrated data rates up to 50 Gbit/s using on-chip antennas," *IEEE Trans. Microw. Theory Techn.*, vol. 65, no. 9, pp. 3312–3323, Sep. 2017.

[30] M. H. Eissa *et al.*, "Wideband 240-GHz transmitter and receiver in BiCMOS technology with 25-Gbit/s data rate," *IEEE J. Solid-State Circuits*, pp. 1–11, 2018.

[31] M. H. Eissa *et al.*, "Frequency interleaving IF transmitter and receiver for 240-GHz communication in SiGe: C BiCMOS," *IEEE Trans. Microw. Theory Techn.*, vol. 68, no. 1, pp. 239–251, Jan. 2020.

[32] J. Grzyb, K. Statnikov, N. Sarmah, and U. R. Pfeiffer, "A broadband 240 GHz lens-integrated polarization-diversity on-chip circular slot antenna for a power source module in SiGe technology," in *Proc. Eur. Microw. Conf. (EuMC)*, Sep. 2015, pp. 570–573.

[33] J. Grzyb, K. Statnikov, N. Sarmah, and U. R. Pfeiffer, "A lens-integrated on-chip circular slot antenna for a 240 GHz power source in SiGe technology," in *Proc. IEEE Int. Symp. Antennas Propag. USNC/URSI Nat. Radio Sci. Meeting*, Jul. 2015, pp. 2055–2056.

[34] Y. P. Zhang and D. Liu, "Antenna-on-Chip and Antenna-in-Package solutions to highly integrated millimeter-wave devices for wireless communications," *IEEE Trans. Antennas Propag.*, vol. 57, no. 10, pp. 2830–2841, Oct. 2009.

[35] G. M. Rebeiz, "Millimeter-wave and terahertz integrated circuit antennas," *Proc. IEEE*, vol. 80, no. 11, pp. 1748–1770, Nov. 1992.

[36] P. Rodriguez-Vazquez, J. Grzyb, N. Sarmah, B. Heinemann, and U. R. Pfeiffer, "A 65 Gbps QPSK one meter wireless link operating at a 225–255 GHz tunable carrier in a SiGe HBT technology," in *Proc. IEEE Radio Wireless Symp. (RWS)*, Jan. 2018, pp. 146–149.

[37] P. Rodriguez-Vazquez, J. Grzyb, N. Sarmah, B. Heinemann, and U. R. Pfeiffer, "Towards 100 Gbps: A fully electronic 90 gbps one meter wireless link at 230 GHz," in *Proc. 15th Eur. Radar Conf. (EuRAD)*, Sep. 2018, pp. 1389–1392.

[38] P. Rodriguez-Vazquez, J. Grzyb, B. Heinemann, and U. R. Pfeiffer, "Performance evaluation of a 32-QAM 1-Meter wireless link operating at 220–260 GHz with a data-rate of 90 gbps," in *Proc. Asia–Pacific Microw. Conf. (APMC)*, Nov. 2018, pp. 723–725.

[39] P. Rodriguez-Vazquez, J. Grzyb, B. Heineman, and U. R. Pfeiffer, "Optimization and performance limits of a 64-QAM wireless communication link at 220-260 GHz in a SiGe HBT technology," in *Proc. IEEE Radio Wireless Symp. (RWS)*, Jan. 2019, pp. 1–3.

[40] P. Rodríguez Vázquez, J. Grzyb, N. Sarmah, B. Heinemann, and U. Pfeiffer, "A 219-266 GHz LO-tunable direct-conversion IQ receiver module in a SiGe HBT technology," *Int. J. Microw. Wireless Techn.*, vol. 10, pp. 1–9, Jun. 2018.

[41] M. R. Khanzadi, D. Kuylenstierna, A. Panahi, T. Eriksson, and H. Zirath, "Calculation of the performance of communication systems from measured oscillator phase noise," *IEEE Trans. Circuits Syst. I, Reg. Papers*, vol. 61, no. 5, pp. 1553–1565, May 2014.

[42] J. Antes and I. Kallfass, "Performance estimation for broadband multi-gigabit Millimeter- and sub-millimeter-wave wireless communication links," *IEEE Trans. Microw. Theory Techn.*, vol. 63, no. 10, pp. 3288–3299, Oct. 2015.

[43] J. Cao *et al.*, "29.2 a transmitter and receiver for 100Gb/s coherent networks with integrated 4×64GS/s 8b ADCs and DACs in 20nm CMOS," in *IEEE ISSCC Dig. Tech. Papers*, Feb. 2017, pp. 484–486.

[44] C.-H. Ahn, S.-W. Oh, and K. Chang, "A dual-frequency omnidirectional antenna for polarization diversity of MIMO and wireless communication applications," *IEEE Antennas Wireless Propag. Lett.*, vol. 8, pp. 966–969, 2009.

[45] K. Pedram, M. Karamirad, and S. M. Husain Ranjbaran, "A novel circular polarization MIMO antenna in 60 GHz technology," in *Proc. IEEE 4th Int. Conf. Knowl.-Based Eng. Innov. (KBEI)*, Dec. 2017, pp. 0335–0338.

[46] S. V. Nesteruk and P. I. Travkin, "Double-polarization antenna for MIMO system of wireless communication," in *Proc. 8th Int. Conf. Antenna Theory Techn.*, Sep. 2011, pp. 214–216.

[47] K. Dasgupta *et al.*, "A 60-GHz transceiver and baseband with polarization MIMO in 28-nm CMOS," *IEEE J. Solid-State Circuits*, vol. 53, no. 12, pp. 3613–3627, Dec. 2018.

[48] K. K. Tokgoz *et al.*, "A 120Gb/s 16QAM CMOS millimeter-wave wireless transceiver," in *IEEE ISSCC Dig. Tech. Papers*, Feb. 2018, pp. 168–170.

[49] J. Grzyb, K. Statnikov, N. Sarmah, and U. R. Pfeiffer, "A wideband 240 GHz lens-integrated circularly polarized on-chip annular slot antenna for a FMCW radar transceiver module in SiGe technology," in *IEEE MTT-S Int. Microw. Symp. Dig.*, Nov. 2015, pp. 1–4.

[50] J. Grzyb, K. Statnikov, N. Sarmah, B. Heinemann, and U. R. Pfeiffer, "A 210–270-GHz circularly polarized FMCW radar with a Single-Lens-Coupled SiGe HBT chip," *IEEE Trans. THz Sci. Technol.*, vol. 6, no. 6, pp. 771–783, Nov. 2016.

[51] S. M. Bowers and A. Hajimiri, "Multi-port driven radiators," *IEEE Trans. Microw. Theory Techn.*, vol. 61, no. 12, pp. 4428–4441, Dec. 2013.
[52] C. A. Balanis, *Antenna Theory: Analysis and Design*. New York, NY, USA: Wiley, 2005.
[53] R. Schmogrow *et al.*, "Error vector magnitude as a performance measure for advanced modulation formats," *IEEE Photon. Technol. Lett.*, vol. 24, no. 1, pp. 61–63, Jan. 2012.
[54] R. Schmogrow *et al.*, "Corrections to 'error vector magnitude as a performance measure for advanced modulation formats' [Jan 1, 2012 61-63]," *IEEE Photon. Technol. Lett.*, vol. 24, no. 23, p. 2198, Dec. 2012.
[55] A. Georgiadis, "Gain, phase imbalance, and phase noise effects on error vector magnitude," *IEEE Trans. Veh. Technol.*, vol. 53, no. 2, pp. 443–449, Mar. 2004.
[56] R. A. Shafik, M. S. Rahman, and A. R. Islam, "On the extended relationships among EVM, BER and SNR as performance metrics," in *Proc. Int. Conf. Electr. Comput. Eng.*, Dec. 2006, pp. 408–411.
[57] J. Grzyb and U. Pfeiffer, "THz direct detector and heterodyne receiver arrays in silicon nanoscale technologies," *J. Infr., Millim., THz Waves*, vol. 36, no. 10, pp. 998–1032, Oct. 2015, doi: 10.1007/s10762-015-0172-6.
[58] N. Sarmah *et al.*, "A fully integrated 240-GHz direct-conversion quadrature transmitter and receiver chipset in SiGe technology," *IEEE Trans. Microw. Theory Techn.*, vol. 64, no. 2, pp. 562–574, Feb. 2016.
[59] D. Pozar, *Microwave Engineering*, 4th ed. Hoboken, NJ, USA: Wiley, 2011. [Online]. Available: https://books.google.de/books?id=JegbAAAAQBAJ
[60] D. F. Filipovic, S. S. Gearhart, and G. M. Rebeiz, "Double-slot antennas on extended hemispherical and elliptical silicon dielectric lenses," *IEEE Trans. Microw. Theory Techn.*, vol. 41, no. 10, pp. 1738–1749, Oct. 1993.
[61] M. J. M. van der Vorst, P. J. I. de Maagt, and M. H. A. J. Herben, "Effect of internal reflections on the radiation properties and input admittance of integrated lens antennas," *IEEE Trans. Microw. Theory Techn.*, vol. 47, no. 9, pp. 1696–1704, Sep. 1999.
[62] M. J. M. van der Vorst *et al.*, "Effect of internal reflections on the radiation properties and input impedance of integrated lens antennas-comparison between theory and measurements," *IEEE Trans. Microw. Theory Techn.*, vol. 49, no. 6, pp. 1118–1125, Jun. 2001.
[63] E. Ojefors, B. Heinemann, and U. R. Pfeiffer, "Subharmonic 220- and 320-GHz SiGe HBT receiver front-ends," *IEEE Trans. Microw. Theory Techn.*, vol. 60, no. 5, pp. 1397–1404, May 2012.
[64] M. Wickert, S. Samad, and B. Butler, "An adaptive baseband equalizer for high data rate bandlimited channels," in *Proc. Int. Telemetering Conf.*, Oct. 2006, pp. 1–10.
[65] F. Chang, K. Onohara, and T. Mizuochi, "Forward error correction for 100 G transport networks," *IEEE Commun. Mag.*, vol. 48, no. 3, pp. 48–55, Mar. 2010.

Pedro Rodríguez-Vázquez received the M.Sc. degree in telecommunication engineering from the University of Málaga, Málaga, Spain, in 2013.

Since 2014, he has been with the Institute for High-Frequency and Communication Technology (IHCT), University of Wuppertal, Wuppertal, Germany, as a Research Assistant. His research interests are in the area of material characterization and communications circuits at submillimeter-wave and terahertz frequencies toward 6G.

Janusz Grzyb received the M.Sc. degree *(cum laude)* in electronic engineering (with a major in the synthesis and design of analog CMOS and BiCMOS circuits with an individual study program) from the Integrated Circuits Laboratory, Gdańsk University of Technology, Gdańsk, Poland, in 1998, and the Ph.D. degree from the Swiss Federal Institute of Technology, Zurich, Switzerland, in 2004.

In 1999, he joined the Electronics Laboratory, Swiss Federal Institute of Technology, where he performed pioneering work in the area of low-cost large-area panel processing multichip-module-based system in package solutions for 60-, 77-, and 94-GHz applications. He was a Research Assistant with the Gdańsk University of Technology from 1998 to 1999. From 2004 to 2006, he was with the Communication System Design and High-Speed/Optical Packaging Groups, IBM T. J. Watson Research Center, Ossining, NY, USA, where he was involved in the development of the low-cost packaged highly integrated SiGe transceiver for 60-GHz Gb/s wireless data communication. From 2006 to 2009, he was with the Research and Development Group, Huber & Suhner, Zurich, Switzerland, where he brought onto the market one of the world's first commercially available point-to-point 60-GHz links: the Sensity Link System. Since 2009, he has been with the Institute for High-Frequency and Communication Technology, University of Wuppertal, Wuppertal, Germany. His current research interests include all aspects of silicon-integrated terahertz electronics.

Dr. Grzyb was a co-recipient of the 2006 Lewis Winner Award for Outstanding Paper of the IEEE International Solid-State Circuit Conference, the 2006 IBM Pat Goldberg Memorial Best Paper Award, the 2012 and 2018 Jan Van Vessem Award for Outstanding European Paper of the IEEE International Solid State Circuits Conference, the 2014 Best Paper Award of the European Conference on Antennas and Propagation, and the Microwave Prize 2017 of the IEEE Microwave Theory and Techniques Society.

Bernd Heinemann received the Diploma degree in physics from Humboldt Universität zu Berlin, Berlin, Germany, in 1984, and the Ph.D. degree in electrical engineering from Technische Universit ät Berlin, Berlin, in 1997.

He joined the IHP GmbH (now Innovations for High Performance Microelectronics), Frankfurt, Germany, in 1984. From 1984 to 1992, he contributed to the development of an epi-free 0.8-μm BiCMOS technology. Since 1993, he has been a member of a team working on the exploration and technological implementation of SiGe HBTs. His research interests include the development and characterization of MOS and bipolar devices.

Ullrich R. Pfeiffer (Fellow, IEEE) received the Diploma degree in physics and the Ph.D. in physics from the University of Heidelberg, Heidelberg, Germany, in 1996 and 1999, respectively.

In 1997, he worked as a Research Fellow with the Rutherford Appleton Laboratory, Oxfordshire, U.K. From 1999 to 2001, he was working as a Post-Doctoral Researcher with the University of Heidelberg on real-time electronics for particle physics experiments at the European Organization for Nuclear Research (CERN), Switzerland. From 2001 to 2006 he was with the IBM T. J. Watson Research Center, Ossining, NY, USA, where his research involved RF circuit design, power amplifier design at 60 and 77 GHz, high-frequency modeling and packaging for millimeter-wave communication systems. He leads the THz Electronics Group with the Institute of High-Frequency and Quantum Electronics, University of Siegen, Germany, in 2007. Since 2008, he has been holding the High-frequency and Communication Technology Chair with the University of Wuppertal, Wuppertal, Germany. His current research includes silicon radio-frequency integrated circuits (RFICs) for mmWave/THz communication, radar, and imaging systems.

Dr. Pfeiffer received the European Young Investigator Award in 2007. He was a co-recipient of the 2004 and 2006 Lewis Winner Award for Outstanding Paper at the IEEE International Solid-State Circuit Conference, the 2006 IBM Pat Goldberg Memorial Best Paper Award, the 2008 EuMIC Best Paper Award, the 2010 EuMC Microwave Prize, the 2014 EuCAP Best Paper Award, and the 2017 Microwave Prize, the 2012 and 2018 Jan Van Vessem Award for Outstanding European Paper at the IEEE International Solid-State Circuit Conference. He has been a Distinguished Lecturer for the IEEE Solid-State Circuits Society and the President of the German Association for Electrical Engineering and Information Technology e.V. (FTEI).